PL-TR-95-2116

ANALYSIS OF IONOSPHERIC MONITORING SYSTEM (IMS) TOTAL ELECTRON CONTENT (TEC) DATA AND EQUATORIAL PHASE-SCINTILLATION DATA

James A. Secan
C. Charley Andreasen
Edward J. Fremouw
Elizabeth Holland
Andrew Mazzella

Northwest Research Associates, Inc.
PO Box 3027
Bellevue, WA 98009-3027

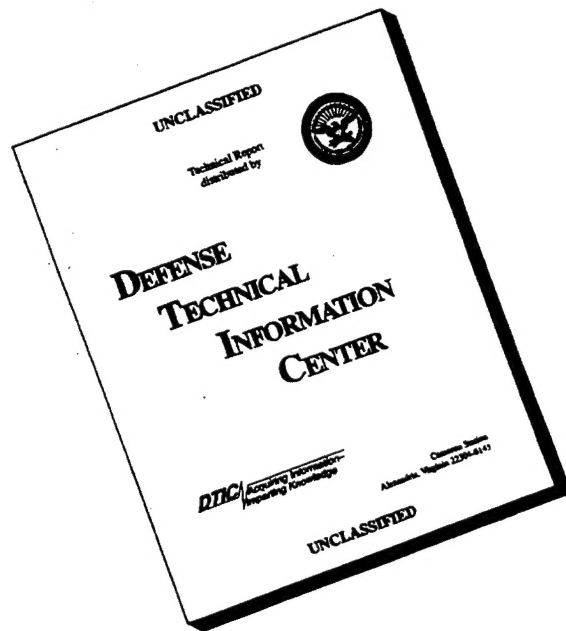1 July 1995

Scientific Report No. 1

DTIC QUALITY INSPECTED 2

Approved for public release; distribution unlimited

19960408 108

PHILLIPS LABORATORY
Directorate of Geophysics
AIR FORCE MATERIEL COMMAND
HANSCOM AIR FORCE BASE, MA 01731-3010

DISCLAIMER NOTICE

UNCLASSIFIED

Technical Report
distributed by

**DEFENSE
TECHNICAL
INFORMATION
CENTER**

DTIC Acquiring Information—
Imparting Knowledge

Cameron Station
Alexandria, Virginia 22304-6145

UNCLASSIFIED

THIS DOCUMENT IS BEST
QUALITY AVAILABLE. THE
COPY FURNISHED TO DTIC
CONTAINED A SIGNIFICANT
NUMBER OF PAGES WHICH DO
NOT REPRODUCE LEGIBLY.

"This technical report has been reviewed and is approved for publication"

GREGORY J. BISHOP
Contract Manager

EDWARD J. BERGHORN
Branch Chief

WILLIAM K. VICKERY
Division Director

This document has been reviewed by the ESC Public Affairs Office (PA) and is releasable to the National Technical Information Service (NTIS).

Qualified requestors may obtain additional copies from the Defense Technical Information Center. All others should apply to the National Technical Information Service.

If your address has changed, or if you wish to be removed from the mailing list, or if the addressee is no longer employed by your organization, please notify PL/IM, 29 Randolph Road, Hanscom AFB, MA 01731-3010. This will assist us in maintaining a current mailing list.

Do not return copies of this report unless contractual obligations or notices on a specific document requires that it be returned.

REPORT DOCUMENTATION PAGE

Form Approved
OMB No. 0704-0188

1. AGENCY USE ONLY *(Leave blank)*	2. REPORT DATE	3. REPORT TYPE AND DATES COVERED
	1 July 1995	Scientific No. 1

4. TITLE AND SUBTITLE

Analysis of Ionospheric Monitoring System (IMS) Total Electron Content (TEC) Data and Equatorial Phase-Scintillation Data

5. FUNDING NUMBERS

F19628-94-C-0067
PE
PRIMSP
TAGH
WVAA

6. AUTHOR(S)

James A. Secan, C. Charley Andreasen, Edward J. Fremouw, Elizabeth Holland, Andrew Mazzella

7. PERFORMING ORGANIZATION NAME(S) AND ADDRESS(ES)

Northwest Research Associates, Inc.
300 120th Ave NE, Bldg 7, Ste 220
P.O. Box 3027
Bellevue, WA 98009-3027

8. PERFORMING ORGANIZATION REPORT NUMBER

NWRA-CR-95-R143

9. SPONSORING / MONITORING AGENCY NAME(S) AND ADDRESS(ES)

Phillips Laboratory
29 Randolph Road
Hanscom AFB, MA 01731-3010
Contract Manager: Greg Bishop/GPIA

10. SPONSORING / MONITORING AGENCY REPORT NUMBER

PL-TR-95-2116

11. SUPPLEMENTARY NOTES

These studies will benefit the AF Space Forecast Center (50th Weather Squadron, AFPCS) by improving undertanding of the behavior of ionospheric structure than can affect operations of various DOD customers.

12a. DISTRIIBUTION / AVAILABILITY STATEMENT

Approved for public release; distribution unlimited

12b. DISTRIBUTION CODE

13. ABSTRACT (Maximun 200 words)

Many military systems used for communications, command and control, navigation, tracking, and surveillance depend on reliable and relatively noise-free transmission of radiowave signals through the earth's ionosphere. These systems can be affected by both large-scale features (> 1,000 km) and small-scale structures (> few hundred km) in the ionosphere, often leading to degraded operations. This report documents the results of the first year of a three-year investigation of various facets of this problem. Two study areas are reported on: (1) an investigation of methods for using signals from Global Positioning System (GPS) satellites to measure ionospheric Total Electron Content (TEC), and (2) a study of the shape and behavior of the phase-scintillation power-density spectrum (PDS) over a scale-size range of 10s to 100s of kilometers. The TEC studies are still on-going; the phase PDS study found that the slope of the phase PDS at these scale sizes is steeper than those found in earlier studies at shorter scales.

14. SUBJECT TERMS

Ionosphere, Ionospheric density irregularities, Ionospheric Total Electron Content, Ionospheric modeling, Scintillation

15. NUMBER OF PAGES

50

16. PRICE CODE

17. SECURITY CLASSIFICATION OF REPORT	18. SECURITY CLASSIFICATION OF THIS PAGE	19. SECURITY CLASSIFICATION OF ABSTRACT	20. LIMITATION OF ABSTRACT
Unclassified	Unclassified	Unclassified	SAR

CONTENTS

Tables

THIS PAGE INTENTIONALLY LEFT BLANK

PREFACE

This report summarizes the work completed during the first year of a project focused on studies of the effects of the earth's ionosphere on transionospheric radiowave propagation.

We thank Dr. Warren Brown, Sandia National Laboratory, for his discussions pertaining to the behavior of the phase-scintillation PDS at large scales.

THIS PAGE INTENTIONALLY LEFT BLANK

1. Introduction

The overall objective of the various tasks that make up this project is to improve our understanding of ionospheric effects on transionospheric radiowave propagation. The phenomena to be studied cover the full range of scale sizes from tens of meters (scintillation effects) to thousands of kilometers (large-scale TEC effects). The twelve tasks outlined in the proposal for this work [*Fremouw et al.*, 1994] can be grouped into the following six study areas (The tasks in the proposal corresponding to these study areas are indicated in parentheses.):

1. Investigate the logarithmic slope of the phase-scintillation power-density spectrum (PDS) at large scales in the equatorial region. Develop a model for a two-regime power-law PDS based on the results of the investigation and implement it in WB-MOD. (Tasks 1 and 2)

2. Investigate the magnitude and behavior of small-scale phase gradients using the equatorial scintillation data sets built in the first study. Develop algorithms for including the effects of small-scale phase gradients on transionospheric propagation based on the results of the investigation and implement them in the WBMOD ionospheric scintillation model. (Tasks 3 and 4)

3. Develop models consistent with the current propagation algorithm in WBMOD for individual intermediate-scale ionospheric features associated with enhanced scintillation (equatorial depletion plumes, polar patches, auroral boundary blobs). Implement these in WBMOD. (Tasks 5 and 6)

4. Develop techniques for producing short-term forecasts of scintillation effects over large spatial areas, implementing and demonstrating these techniques in computer programs. (Task 7)

5. Deploy, operate, and maintain satellite receiver instrumentation on a long-term basis at local and remote sites to collect databases of ionospheric Total Electron Content (TEC) and scintillation observations. Use these data to (a) analyze performance of ionospheric monitors, (b) validate models of ionospheric behavior, and (c) develop/formulate algorithms to improve the performance of both ionospheric monitors and models. (Tasks 8 and 9)

6. Deploy, operate, and maintain satellite receiver instrumentation on a short-term basis at local and remote sites where unique opportunities exist for enhancement of test data sets, particularly where other instruments have been deployed to collect other ionospheric measurements. Collect these data, and ancillary data from other instrumentation, into documentated data sets that can be used as outlined in the previous study description. (Tasks 8, 9, and 12)

1

[Note: Task 11 is not explicitly included in the above listing as it includes support to all of the various tasks described in the proposal.]

During the first year of this project, we have completed Task 1 and begun work on Tasks 8 and 9. This report documents the results of our efforts.

2. Ionospheric Total Electron Content Studies

Investigations of ionospheric Total Electron Content (TEC) are being performed based on current data acquired from the Air Force Ionospheric Measuring System (IMS) stations being deployed globally, as well as other measurement systems deployed on a temporary or permanent basis. Previously acquired data also are being processed and analyzed to investigate ionospheric conditions at alternative times and locations. The sources of ionospheric measurement data utilized during this period of study encompass the following:

1. IMS stations deployed at Otis Air National Guard Base (ANGB), Massachusetts, and Croughton Royal Air Base, England;

2. A portable single-frequency Global Positioning System (GPS) receiver deployed for an ionospheric study campaign at Agua Verde, Chile, in September and October 1994;

3. Data sets previously recorded at Shemya, Alaska, during 1992 by the Real-Time TEC Monitor developed by the University of Texas Applied Research Laboratory (ARL).

Part of this effort was conducted by RDP, Incorporated, under subcontract to Northwest Research Associates, Inc. (NWRA). Appendix A to this report includes the full text of the final report provided by RDP describing the results of their work. Some of this information is repeated in the body of this report where pertinent.

2.1 General Analysis. Support for satellite and receiver bias calculations was provided using the error-minimization search algorithm and software that were developed during the summer of 1994 [*Bishop et al.,* 1994]. Earlier results were re-evaluated in an attempt to resolve discrepancies between PL Hanscom and JPL Westford data for the same dates (94-114), but no definitive conclusions were obtained. A procedure was developed to plot derived vertical Total Electron Content (TEC) profiles for a set of adjoining latitude bands as part of this investigation. An example of these latitude-band plots is shown in Figure 1.

The database generation, bias calculation, and TEC plotting procedure was standardized for general applicability to multiple receiver sites, using site-specific information in separate files when necessary.

A refined method for bias calculations was developed, replacing the earlier minimization search process by a system of coupled linear equations. The refined method requires only
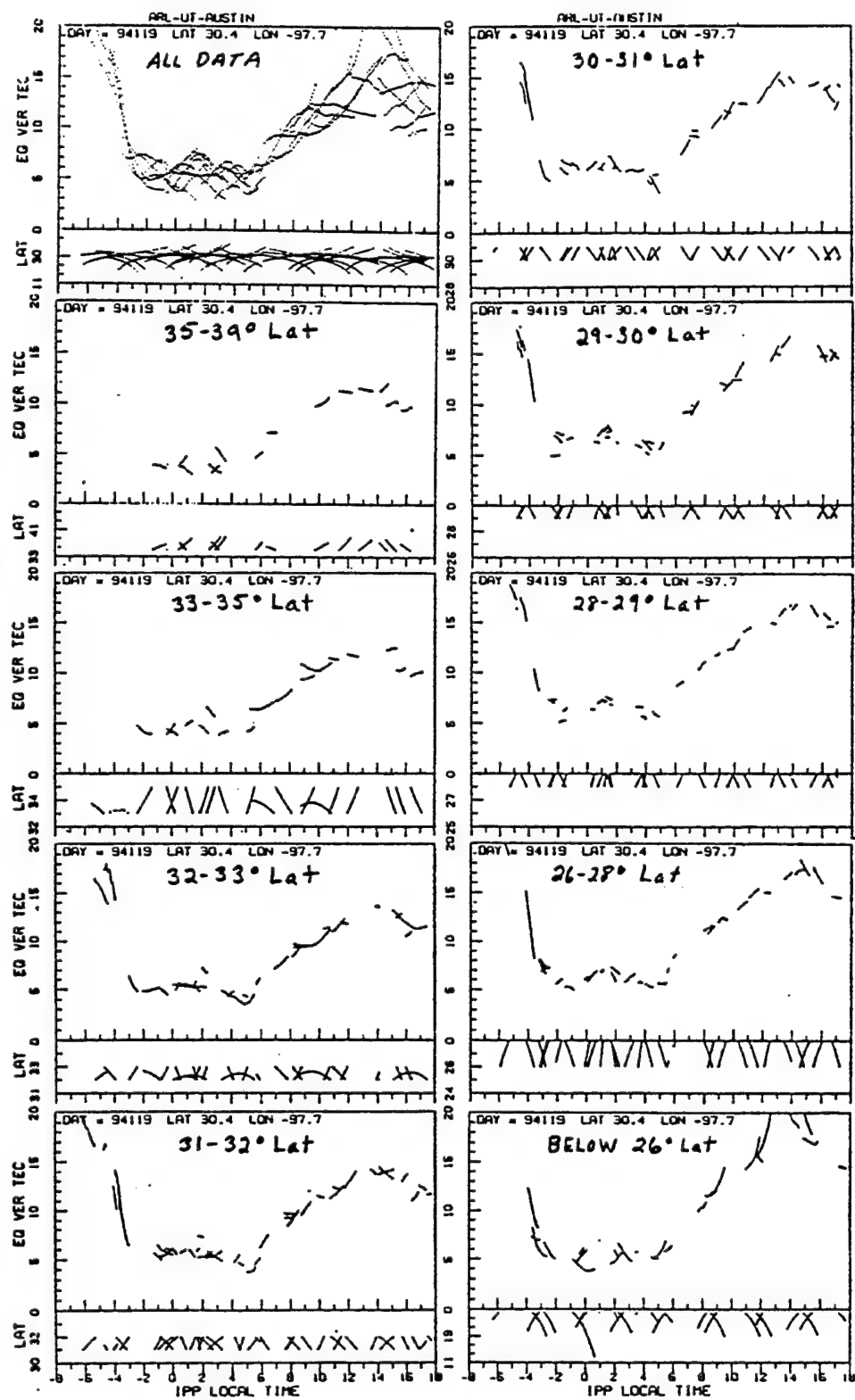
2

Figure 1: Latitude-band plots of equivalent-vertical TEC data for day 119, 1994, collected by Applied Research Laboratories, University of Texas at Austin.

one pass through the data to determine the coefficients and inhomogeneous terms of the linear equations, and significantly reduces the time required to perform the calculation. The refined method was applied to data from the IMS operating at Otis ANGB, to validate its operation.

Further developments were pursued regarding the refinement of the bias calibration method using a wider latitude range. Examination of the standard TEC slant factor, based on the assumption of an infinitesimally thin ionosphere, in comparison to numerical models for a Chapman ionospheric profile indicated an increasing error at lower elevations. Thus, an elevation cut-off of 35° was incorporated into the bias calculation method, together with the wider latitude band and the weighting parameters that emphasized apparent satellite conjunctions in local time and latitude.

The bias-determination process for receiver system calibration was run for day 94-121 data, collected by Applied Research Laboratories at the University of Texas at Austin (ARL). This was an active day (high K_p) and proved difficult to calibrate. The first calibration used the method that constrains measurements in the three-degree overhead latitude band (29°-32°) to agree, if they are close in Ionospheric Penetration Point (IPP) local time. The second run shifted the latitude range for agreement to the less disturbed north (32°-35°). A third run emphasized agreement of satellite measurements at conjunctions over the full range of observation latitudes (11°-49°). While the conjunction approach yielded better results, the disturbed nature of the day and a variety of data anomalies prevented a successful calibration of these data.

Day 94-119 data were obtained from ARL and calibrated using the conjunction method. This calibration resulted in a reasonable diurnal profile for the data, but a few small data segments did not align with the rest of the data. Each data segment was then plotted and examined for data quality, specifically: continuity, duration, elevation, and multipath content. Small segments of less than one and one-half hours duration, low-elevation segments, and high-multipath segments were removed. The absolute levels of these types of segments are often incorrect due to the multipath component of the group delay biasing the phase-averaging process. The calibration results of the edited data are shown in Figure 2. These agree well with ARL's independent calibration of the same system.

A package of software with the potential capability of allowing remote access and remote control of a Windows-NT microcomputer was acquired and tested. The remote-access capabilities were encouraging, but the remote-control capabilities were inadequate. Acquisition and implementation of such a software package with both capabilities would allow Windows-NT to be the standard operating system for the remote PC data-collection stations as well as for the local data-processing systems.

The standard plotting program for displaying diurnal vertical TEC profiles was enhanced to allow individual colors to be used for identifying the satellites observed during the day. Because of the limited selection of available colors, compared to the larger number of satellites
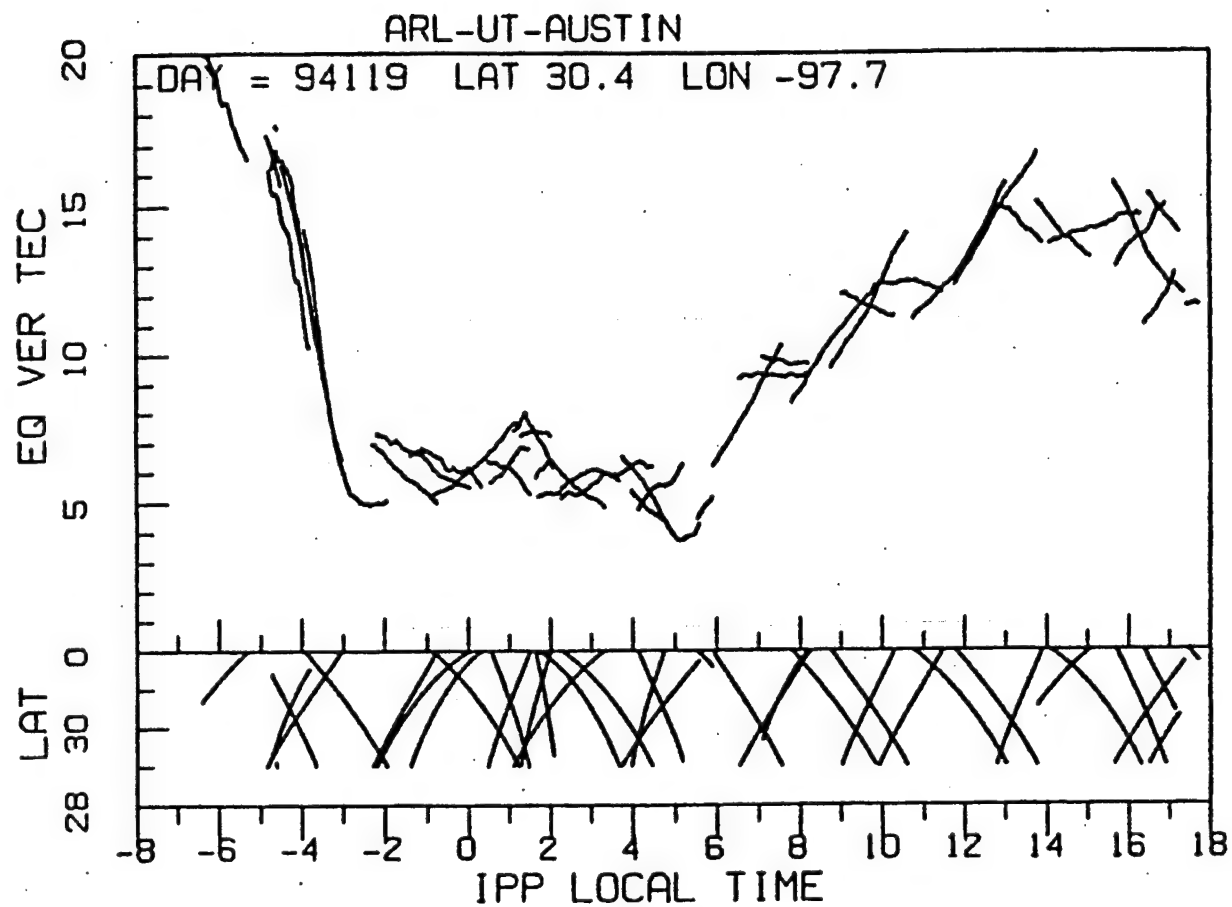
Figure 2: Result of bias calibration with conjunction emphasis for data collected on day 11, 1994, by Applied Research Laboratories, University of Texas at Austin.

observed, a review of the observing pattern for satellites was performed to ensure that satellites with overlapped time coverage were displayed with distinct colors. This plotting format was used to diagnose apparent anomalies in the diurnal profiles derived from GPS observations.

This plotting program was also adapted for use with single-frequency TEC databases and was utilized to plot abutting segments of consecutive days of dual-frequency TEC data for an Ashtech receiver operated at Phillips Laboratory at Hanscom (PLH) in April 1994, where each day was associated with its own bias determination. The transitions in equivalent vertical TEC at the day boundaries were seen to be continuous.

2.2 Ionospheric Measuring System (IMS). A number of investigations were performed to evaluate the results from the IMS at Otis and to improve the processing of data from that system. The general data-listing program was modified to report the satellite and receiver biases in nanoseconds of delay, with provisions to select any of the three data record types (raw data, 1-minute data, or 15-minute data) individually or jointly. This program was utilized to determine the cause of anomalously high TEC values appearing in the 15-minute reports being transmitted to the Air Weather Service, and to validate the usage of the satellite and receiver biases in the reported slant and vertical TEC values.

As a consequence of these investigations, the satellite and receiver biases were added as output values to the conversion program that generates the initial data files for the bias determination process, although the complete utilization of these biases has not yet been implemented. Some of the anomalous TEC values were attributed to significant initial discrepancies in the measured differential group delay, contributing to a major phase averaging error, which diminished with time, but other unusual TEC values were associated with spurious satellite observations, which provisionally have been dubbed "ghosts". A preliminary characterization of these has been developed, but further investigation is required.

A set of satellite and receiver biases was defined for the Otis IMS on 13 February 1995, using measurements performed on 23 January 1995. A plot of data employing these biases is shown in Figure 3. These biases were derived using the bias-determination method to calculate correction values for the initial biases established for the IMS, with the appropriate transformation for transmitter group delay being applied to the satellite biases. The resulting TEC values were monitored on several subsequent dates, using procedures similar to those in processing the data for bias determinations, and the results were generally reasonable. Data files for 3 April 1995 were retrieved from the IMS at Otis and were used to further evaluate the performance of the earlier bias definitions for the Otis IMS and to calculate corrections and revised bias values for installation on the Otis IMS. These data have also been reviewed for anomalous and spurious TEC measurements, as part of the continued assessment of the IMS performance.

UNIX scripts were developed for manual daily data-file transfers from the IMS to its companion PC and for automated real-time transfers from the IMS to the PC. The real-
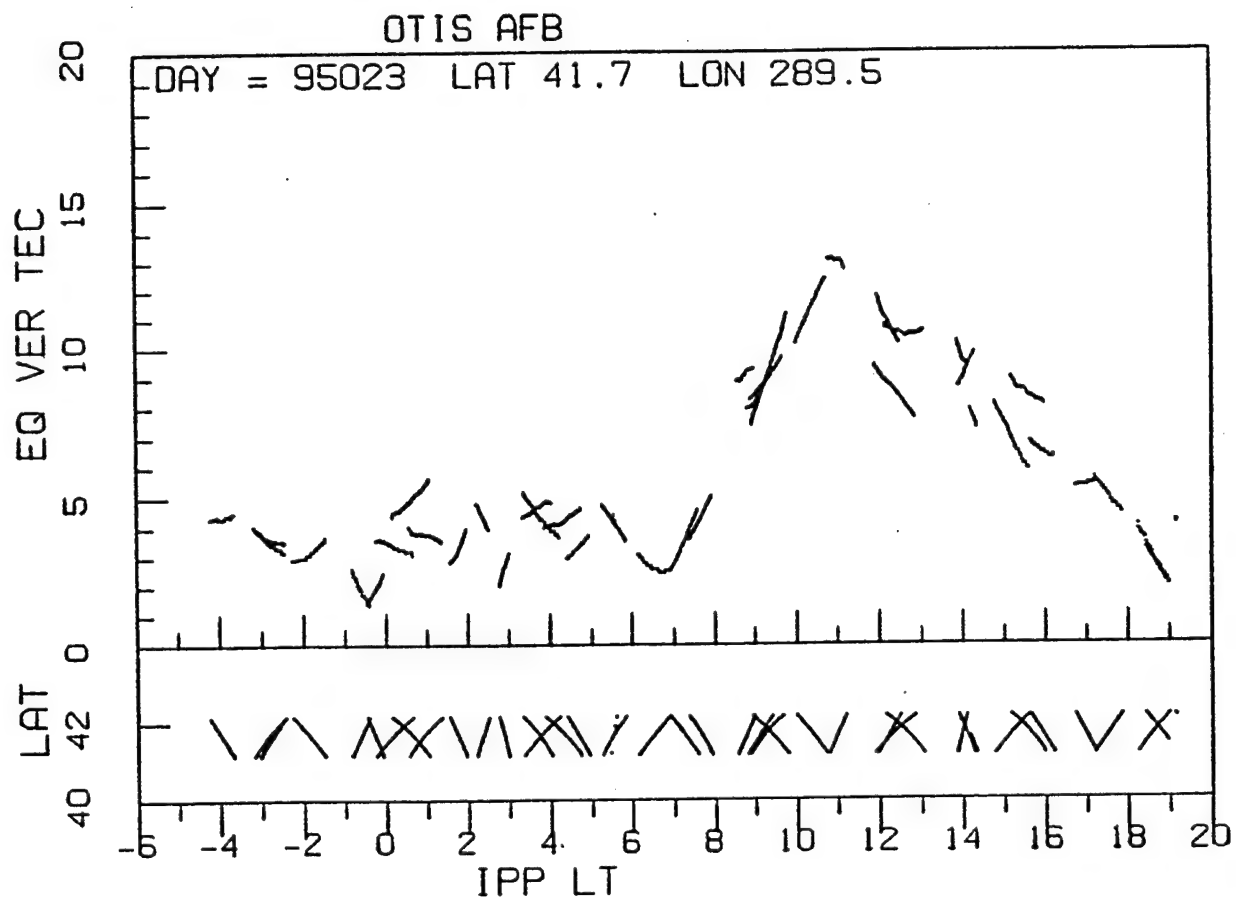
Figure 3: One-degree "overhead" plot of IMS data from Otis ANGB, MA, after bias calibration.

time transfer process was tested for about three weeks at Otis ANGB, and requires some refinement to interact reliably with the PC FTP server.

Data continue to be collected by the IMS at Otis ANGB, MA. Data files for the period 27 December 1994 to 27 June 1995 were transferred from the Otis IMS to the companion PC for that site, and files up to 25 June 1995 have been archived to tape for transfer to PLH.

The IMS at Croughton RAF base in England has been checked since returning to functional status on 2 June 1995. The companion PC for that site was not initially operational, requiring a reconfiguration of the network software before data-transfer operations could occur. On-line data file-storage procedures were installed on the IMS, to preserve data files in the absence of an operational UNIX tape-archiving process.

An extensive review has been performed for the Otis IMS 15-minute data, using files from days 93, 94, 106, and 157 of 1995 (3 April, 4 April, 16 April, and 6 June). Plots of the TEC data were generated, showing the occurrence of extreme outliers [several hundred TEC units (one TEC unit = 10^{16} electrons/m^2), positive or negative]. The outliers were essentially eliminated by excluding the first three 15-minute samples of each satellite pass, as well as by excluding all negative TEC values.

Data collected in 1995 from days 001-004, 006, and 008-014 collected by the IMS system at Otis ANGB were processed for comparison to concurrent radar measurements. The quality of every pass was examined, and the data were edited to remove short segments, low elevation segments, and outliers. Each day was calibrated using the bias algorithm emphasizing satellite conjunctions. Files containing date, time, azimuth, elevation, and slant TEC were generated from the calibrated data. These files contain data from time intervals concurrent with the radar observations, with an additional half-hour of data on each end of the interval. The calibrated data files for days 013 and 014 have been made available to personnel working for PL/GPIM, and the remaining data will be delivered soon. The associated radar data files, originally obtained from MITRE, were also delivered.

The detailed data examination of the January 1995 Otis IMS data revealed the occurrence of a "ghost" GPS satellite immediately prior to the data record for an actual GPS satellite (PRN-12) at about 12:00 UT on 12 January 1995. The "ghost" for PRN-12 initially appears at high elevation, at the same location as PRN-26, after which the data sequence makes an abrupt change to the actual location for PRN-12, near the horizon, with a continuous differential phase delay but a jump in the differential group delay. Other "ghost" GPS satellites were observed at about this time, as indicated by reported ephemeris parameters. The mechanism for "ghost" occurrence remains to be determined, but the occurrence and general nature of the "ghost" GPS satellites have been reported to the original IMS development team at Draper Laboratories.

A spreadsheet was prepared to summarize the bias-calculation results for the January 1995 data that was processed from the Otis IMS. An overall variation of about 3 TEC units was observed for the 12 days processed, with a standard deviation of about 0.9 TEC units.

Investigations are in progress to determine whether this is a true instrumental variation, a consequence of data anomalies, or a limitation of the analysis.

As a potential remedy for the overseas IMS data-report transmission difficulties, a PC program was developed to generate Total Electron Content and Scintillation Code (TELSI) messages from the 15-minute data files, and a supervisory script for this program was also created, to initiate the generation of a TELSI message upon arrival of a new data file at the PC from the network connection to the associated IMS. A dialup capability to the PC would then allow the TELSI message to be acquired by a domestic PC and transmitted using the domestic weather network. Sporadic difficulties with the automated data transfer from the IMS to its companion PC, as well as the lack of a direct dialup line and local network port for this purpose, have impeded further development of this procedure.

To facilitate the examination of data from the IMS, a program was developed to plot the one-minute data samples for differential group delay or differential phase delay. This program was used in an interactive mode to examine the data sets used for the radar comparison study.

To enable a more extensive review of the 15-minute IMS data reports, the data-listing program was augmented to include the average equivalent vertical TEC, in addition to the maximum and minimum TEC values. The ephemeris data reporting was also augmented and incorporated as a separate option, to facilitate the examination for "ghost" satellite occurrences.

A summary log has been developed for the IMS at Otis, primarily to monitor the duration of operations for each of the two UNIX computer systems in the IMS. This log has been regularly reviewed and updated, and a recent version was presented to the original IMS development team at Draper Laboratories.

2.3 Model Comparisons for Shemya Data. The bias-determination procedure was applied to a number of days of data from Shemya, AK, from 1992 to test the method for ionospheric characteristics for this site and to corroborate earlier results derived by a different technique. Some parametric revisions for the Ionospheric Penetration Point (IPP) latitude range and observation-conjunction weighting were required to appropriately associate measurements from all of the observed GPS satellites, but the method produced excellent results.

These Shemya data were collected using the TI-4100 four-channel GPS receiver deployed as the ARL Real-Time Monitor. The data files required conversion from the four-channel format to pass-file format for input to the bias-determination process. Once calibrated by this process, these data were used in a comparative assessment of the measured TEC versus TEC as predicted by the Bent model.

2.4 Single-Frequency Ionospheric Measurements. The differential carrier phase and differential group delay data from the Otis IMS GPS measurements were used in a simulation of single-frequency bias determination. The slant TEC from differential carrier phase, which is only a measure of relative slant TEC, was input to the single-frequency calibration process.

9

The resulting diurnal profile for equivalent vertical TEC was within approximately 2.5 TEC units of that derived from phase-averaged data, which utilizes the absolute differential group delay as a reference. A similar experiment was performed using slant TEC from differential group delay, which is significantly contaminated by noise and multipath, and therefore more closely simulates the single-frequency data in this regard. These data were smoothed using a sliding-average process to decrease noise and multipath and were then input to the calibration process for single-frequency data, as individual satellite passes. Despite a resultant noise level of about 6 TEC units, a rough diurnal profile is apparent, although quantitative agreement with the dual-frequency TEC calculation is only 3-5 TEC units, with a total diurnal TEC modulation of only about 15 TEC units.

Data collected with the Trimble Pathfinder single-channel GPS receiver were used to study the adaptation of the bias-determination process for use with single-frequency GPS measurements. Relative slant-path TEC can be determined according to the following equation:

$$\mathrm{TEC}(t) = \frac{\kappa}{2}\left(\frac{R(t)}{c} - \frac{1}{f_l}\int_0^t \Delta f(\tau)d\tau\right) \tag{1}$$

where R is the pseudo-range, Δf is the Doppler frequency, c is the speed of light, f_l is the carrier frequency, and κ is a conversion factor (time delay to TEC units) which is equal to 1.845 TEC units/nanosecond.

The time tag on the data as extracted from the binary records using Trimble's utility program for conversion to ASCII was not precise enough to produce data that could be used for these studies. Trimble provided us with a new program to extract ASCII records from the binary data, giving the time to three decimal places. A program to read this new ASCII format data and extract individual satellite pass files was written, and the slant TEC was recalculated and plotted. These results were compared to slant TEC calculated from dual-frequency differential data, and the values for some satellite observations were found to diverge, although others showed good agreement. Analysis of this problem is continuing, but a jitter in the reported time tags is suspected.

Trimble data collected during September and October 1994 were examined to determine if scintillation can be seen. These data contain multipath effects from the receiver antenna's environment. The template method is being used to remove the multipath content. First, a quiet day of data is chosen to be used as the template. A processing program is applied that reads a Trimble satellite pass file, converts the signal-to-noise ratio in antenna measurement units (AMU) to decibels, smooths the data by taking a sliding average over a user-specifiable number of points, and converts from decibels back to AMU, writing the data to an output file. These data become the multipath template for that satellite. The template is applied to another pass with apparent scintillation signatures. A second program applies the template to a subject file by time-shifting the template to align with the time of the subject file,

10

and removes the multipath, point by point, by subtracting the template from the subject file. If the time correspondence of the two files is not exact, this program will interpolate a template value from the existing template points that bracket the subject data point in time. A sample of the original signal profile is displayed in the upper frame of Figure 4, while the same data with the multipath effects removed are displayed in the lower frame of Figure 4.

Two days of Trimble signal data recorded during the Chile campaign of September-October 1994 (94-274, 94-276) were processed for multipath compensation, using the adjacent days (94-273, 94-275) to generate the multipath template. Except for isolated instances of severe multipath signal attenuation, the results were excellent.

A further analysis of the 1994 Chile data was performed in which the pseudo-range and Doppler data were utilized to calculate relative slant TEC, over the same intervals as the signal amplitude data which was corrected for multipath. Although the long-term variation of the slant TEC values being calculated is believed to contain significant errors, the short-term variation is regarded as reliable. A significant temporal correlation was observed between the occurrence of scintillation in the signal amplitude data and TEC depletions along the same line-of-sight.

3. Analysis of Equatorial Scintillation Data

The objective of study area #1 is to determine whether the slope of the PDS [on a log(PSD) vs. log(f) plot] is steeper at scale-sizes on the order of a few tens of kilometers than over the scale-size range covered in the original analysis of Wideband data collected at Ancon and Kwajalein. The original analysis fit the spectra over the frequency range of 0.5 to 10.0 Hz and found that the slope of the PDS in this range is roughly 2.5. The impetus for the present work was a set of spectra collected in the equatorial region that showed slopes on the order of 3.5 to 4.0 over a range of scales corresponding to spectral frequencies below the frequency range covered in the Wideband analysis [*W. Brown,* private communication]. The goal of this effort is to reconcile these observations, if possible.

There are several possible sources/explanations for this disagreement:

1. The phase-scintillation PDS may steepen at frequencies below the range covered by the Wideband analysis. Evidence of this has been found in previous studies aimed at reconciling results from the HiLat satellite with those from Wideband. (See Section 3.1 in *Fremouw et al.,* [1989].)

2. Problems in the processing employed in the original Wideband analysis (spectral leakage) led to underestimation of the spectral slope during periods of intense scintillation [*ibid*]. All of the steep-slope examples were taken during times of severe scintillation, situations in which the Wideband processing would have produced slopes that were too shallow.
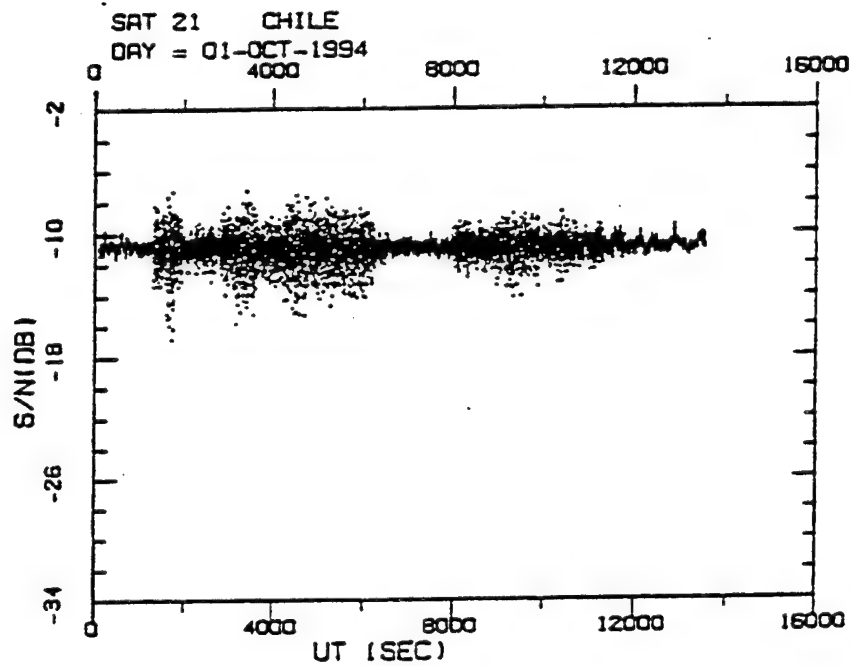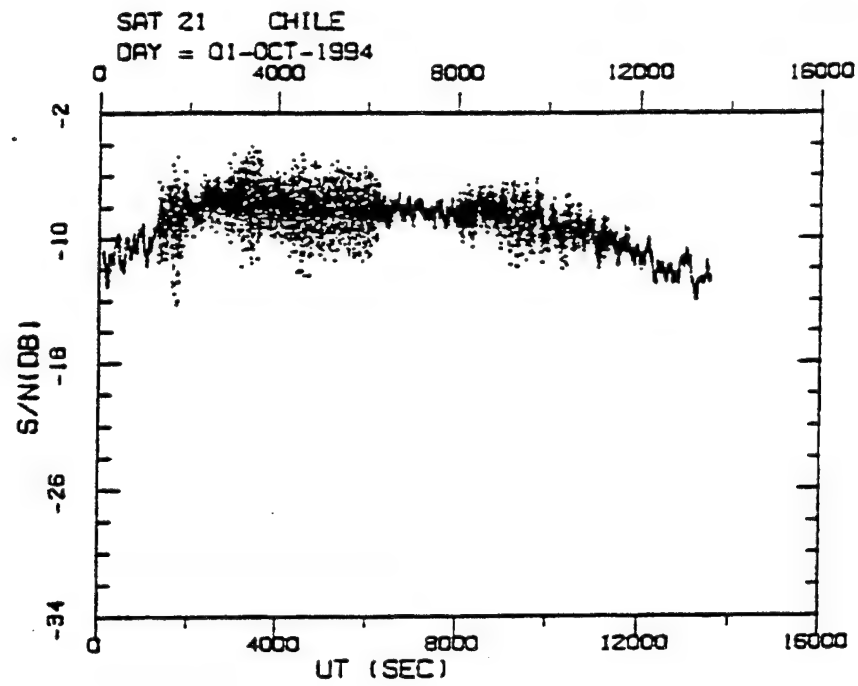
Figure 4: Top: Original signal data for single-frequency GPS receiver. Bottom: Signal data for single-frequency GPS receiver with multipath effects removed.

3. The *in-situ* spectrum of the plasma-density irregularities that are the cause of scintillation may be anisotropic in much the same way in which the shapes of the irregularities are. All of the Wideband data were collected in passes that scanned north-south (night) or south-north (day), approximately along the geomagnetic meridian. The data from which the steep slopes were derived were taken from a system with a velocity vector at an appreciable angle to the local geomagnetic meridian. Given the fact that the large depletion-plume structures that cause the severe post-sunset scintillation are aligned with the geomagnetic field direction, it would not be surprising that the spectrum, particularly at the large-scale end, was anisotropic.

4. The Wideband satellite was sun-synchronous, with the night passes at Ancon and Kwajalein occurring four to five hours after local sunset. In our recent upgrade to WBMOD [*Secan et al.,* 1993], we found that the equatorial scintillation has a sharp onset shortly after local sunset, reaches its peak levels within an hour or so, and is in decay by four to five hours after sunset. It is certain that the spectrum evolves with time, and may look quite different in its decay phase (when it was sampled with Wideband) than in its growth and peak phases. It appears that at least a few of the steep-slope examples were from times just after local sunset [*W. Brown,* private communication].

It was our intent to address as many of these issues as possible given the constraint that no further data may be collected.

The plan of attack was to reprocess a selected sub-set of the Wideband data collected at Ancon and Kwajalein and all of the data collected from HiLat and Polar BEAR during the 1986 and 1988 DNA-sponsored PEAK campaigns at Kwajalein. The data were all processed using a common set of procedures distilled from the original processing procedures used for these data. The raw Wideband data (including all 12 channels of beacon data) were provided by Mission Research Corporation (Dr. Dennis Knepp) and constitute a set of 49 passes (21 from Ancon, 28 from Kwajalein). The raw HiLat and Polar BEAR data from the two PEAK campaigns were taken from the NWRA archives, and constitute a set of 40 HiLat passes (13 from PEAK 86; 27 from PEAK 88) and 28 Polar BEAR passes (all from PEAK 88). A full listing of the passes used in this analysis is given in Appendix B.

All of the raw pass files from all three satellites (Wideband, HiLat, and Polar BEAR) and the software required to retrieve, reformat, and process the data have been written to a long-term archive on optical read/write disks. In addition, the data and software have been archived on Exabyte 8mm disks in Unix `tar` format.

3.1 Data Processing. The initial processing was designed to put the data into common file structures and to generate a first look at spectral behavior at the low-frequency end of the phase spectrum. Software was developed to (1) read the various raw data files (Wideband and HiLat/Polar BEAR), (2) separate out the intensity and phase data for a single channel and resample the data to a common data rate of 125 Hz (Wideband from 500 Hz and HiLat/Polar BEAR from 250 Hz), (3) detrend the VHF phase data by subtracting a trend

13

VHF Reprocessing Results (All)

Average p = 2.26

Linear fit: p = 2.17 - 0.12*log(T)
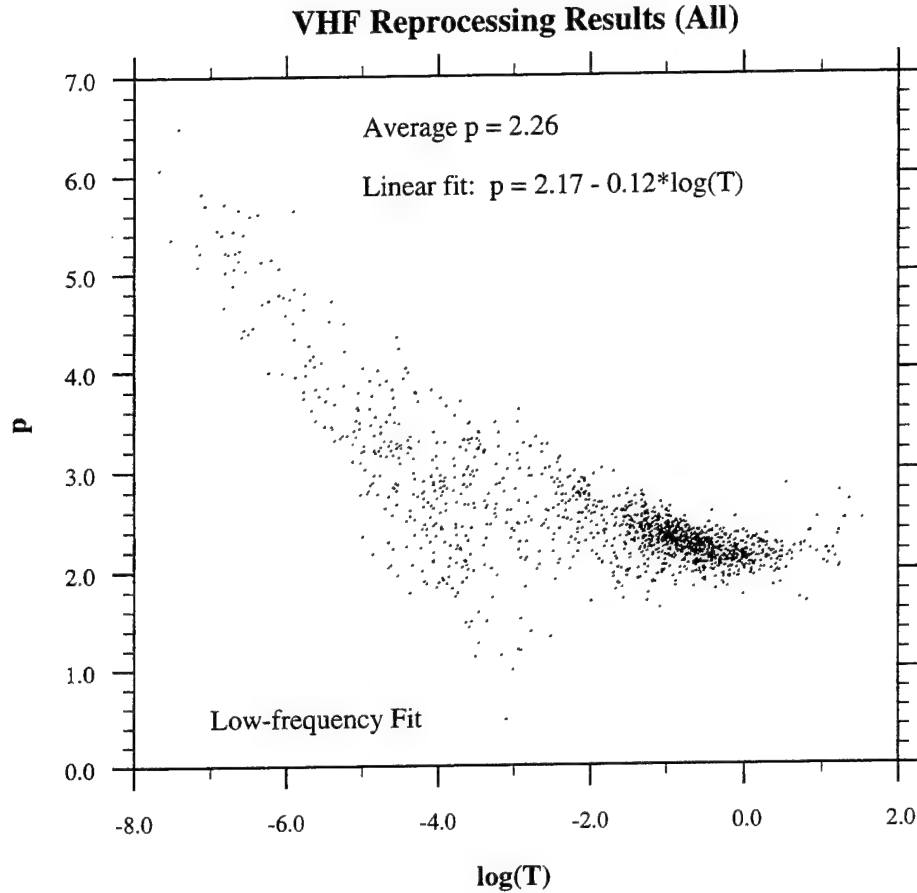
Low-frequency Fit

Figure 5: Scatter plot of the slope of the low-frequency PDS fit (p) as a function of the log of the intercept of the fit (T). The linear fit results relating p to $\log T$ were obtained by fitting over the range $-2.0 < \log T < 2.0$.

derived from the output of a low-pass Butterworth filter with a low-frequency cutoff at 60s (Wideband processing used a 10s cutoff; HiLat/Polar BEAR processing used a detrending procedure equivalent to a 15-20s cutoff), (4) generate spectra from the detrended phase (60 second samples taken every 30 seconds) using a 30% cosine-taper window, and (5) calculate slopes and intercepts for two frequency ranges (lower: 0.03 to 3.0 Hz; upper: 3.0 to 16.0+ Hz). The high-frequency cutoff of the upper section was determined using an algorithm for finding the noise floor of a power-law spectrum used in the HiLat/Polar BEAR processing.

The scatter plot in Figure 5 is representative of the results of this initial processing. This shows the variation of the slope, p, as a function of $log(T)$ from the low-frequency fits for the entire data set (354 data points). Also shown is the average slope for the entire set (2.26) and the equation for a linear least-squares fit to the set. This shows no evidence of a steeper slope at larger scale sizes (lower spectral frequencies). In fact, the average slope

14

is significanlty shallower than the value currently used in WBMOD (2.5). This led us to a complete re-evaluation of the methods we were using to process the data to ensure that we were not masking the effect we were looking for by the way in which the data were being processed.

After extensive experimentation, we settled on the following changes to our processing scheme:

1. Open up the detrender from 60 s to 192 s. This was accomplished by removing a linear trend from each sample of undetrended data, constructed by fitting a straight line to the first and last points in the sample (end matching), and then removing the mean of this "detrended" sample from all points in the sample (mean removal).

2. Generate spectra from 192-s samples.

3. Generate linear fits to the spectra (in log PDS and log frequency) over two frequency ranges: 0.01 to 0.1 Hz and from 0.1 to 1.0 Hz. The resulting slope and intercept parameters are denoted T_l and p_l for the first (low frequency) range and T_h and p_h for the second (high frequency) range. Note that we have defined the intercept parameters as the power spectral density (PSD) values at frequencies in the center of the (log) range of the fits. Thus, T_l is the PSD at $\log f = -1.5$ as derived from the fit to the low-frequency section, and T_h is the PSD at $\log f = -0.5$ from the fit to the high-frequency section.

We also determined that we needed to move from VHF to L band, which limited us to the Wideband passes as both HiLat and Polar BEAR used L band for the phase reference so that only intensity data are available at L band from these data sets. Before presenting the new results, we will discuss the basis for the changes made in the processing procedures.

The move from VHF to L band was initially to move closer to the frequencies at which the Brown data were taken. As we will show later, this move also removed propagation effects from the phase spectra (diffraction and strong scatter). We will present results from both VHF and L band, but the analysis will focus on the L band results. This also limited us to the Wideband data (roughly half of the data available), but this did not prove to be a problem in terms of the goal of this task.

The use of a longer data sample and a longer period on the detrender is somewhat self-explanatory. Our goal in this analysis is to look at the largest scale sizes that we can without seriously compromising our assumptions of stationarity in each data sample. The selection of a 192-s sample size was a trade-off between a desire to open the detrender as wide as possible and the requirement for nominal stationarity within each sample. This also permitted us to have between four and seven spectra from each pass (overlapping 192-s samples).

We were concerned about the impact of various steps in the data processing on the slopes of the spectra, particularly to the low-frequency regime. The processing steps invariably involve a trade-off between altering the data as little as possible (to avoid the introduction

15

Table 1: Results of the processing analysis. The values listed for T and p are the average over the set $\pm$ one standard deviation. The entries in the "Detrend" column denote the low-pass filter detrend (LP) or the end-match/mean-removal detrend (EMMR).

		Low-frequency Regime		
Case	Detrend	Window	T_l	p_l
1	LP	YES	6.92 ± 8.0	3.56 ± 0.90
2	EMMR	YES	9.78 ± 6.7	4.18 ± 0.98
3	EMMR	NO	9.91 ± 6.6	3.99 ± 0.74
		High-frequency Regime		
Case	Detrend	Window	T_h	p_h
1	LP	YES	-20.95 ± 9.8	2.91 ± 0.65
2	EMMR	YES	-20.94 ± 9.8	2.91 ± 0.65
3	EMMR	NO	-20.25 ± 9.0	2.95 ± 0.62

of artifacts) and the need to isolate the signal of interest as cleanly as possible. In order to assess the impact of various processing alternatives, we looked in detail at two of the steps used in the processing: (1) the removal of the phase trend (using a low-pass filter detrender or using an end-matched linear trend), and (2) windowing the data prior to generating the spectra (yes or no).

All of the Wideband L band data were processed using three combinations of these two steps: low-pass filter (LP) and window (denoted Case 1), end-match/mean removal (EMMR) and window (Case 2), and EMMR and no window (Case 3). The resulting values for the slopes and strengths are shown in Table 1. The results in the high-frequency regime are nearly identical among the three methods. Unfortunately, although not surprisingly, the largest differences between the various combinations are in the slopes in the low-frequency regime, the parameter in which we are most interested. Figures 6 and 7 show these results in a bit more detail. These compare the results obtained for each of the four parameters between Case 1 and Case 2 (Figure 6), and Case 2 and Case 3 (Figure 7).

One of our concerns with using the LP (low-pass filter) detrender is its effects on the lowest few spectral bins in the PDS. If the sample size used in creating the PDS is comparable to the cutoff used in the low-pass filter, the lowest-frequency bins in the PDS may be too low. We have seen this effect in several previous analyses of Wideband and HiLat data, and it is apparent again in the lower values for p_l for Case 1.

A second concern is in possible effects, again on p_l, of the windowing procedure. The
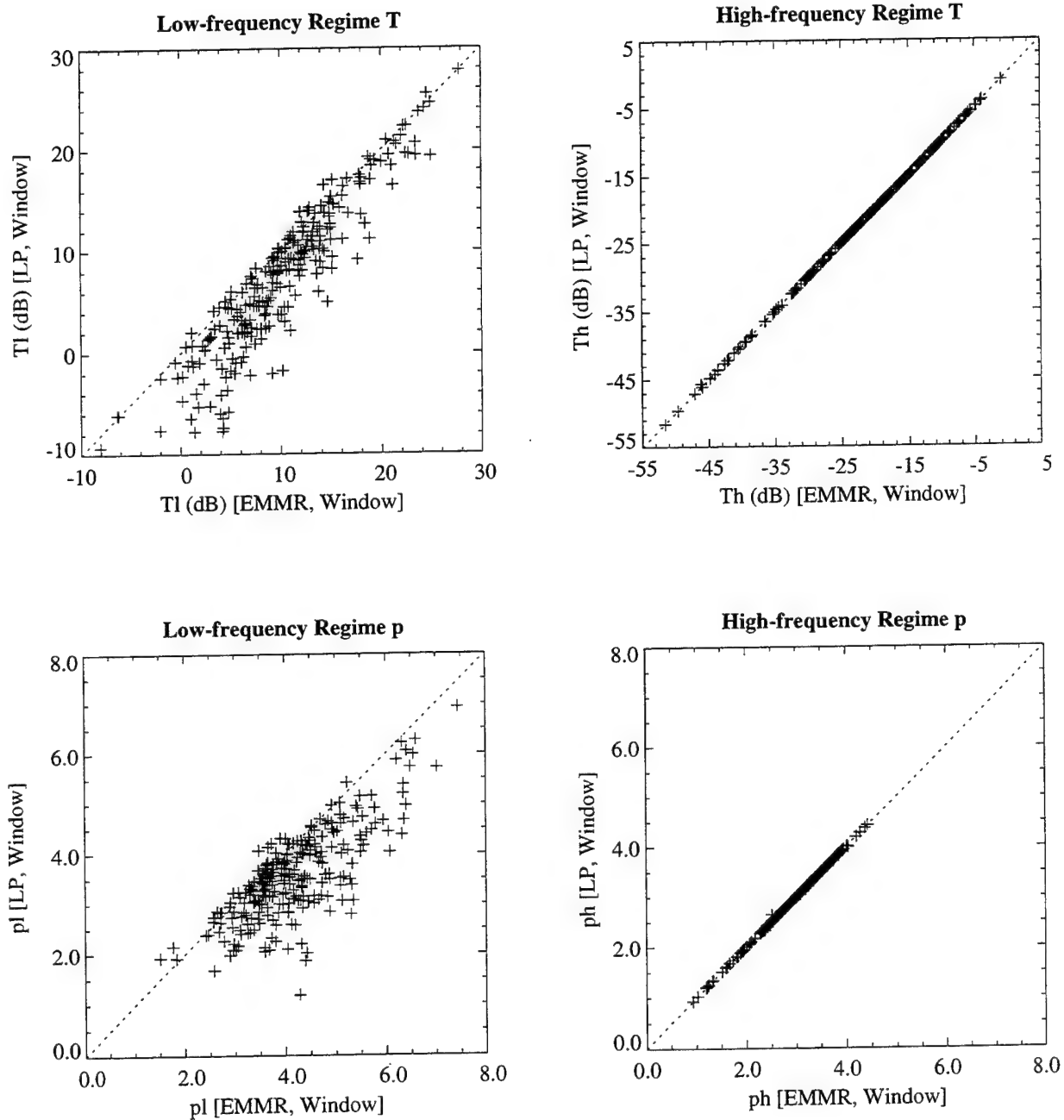
Figure 6: Comparison of strengths (top plots) and slopes (bottom plots) between Case 2 (*EMMR,* window; *x* axis) and Case 1 (*Detrend,* window; *y* axis) processing.
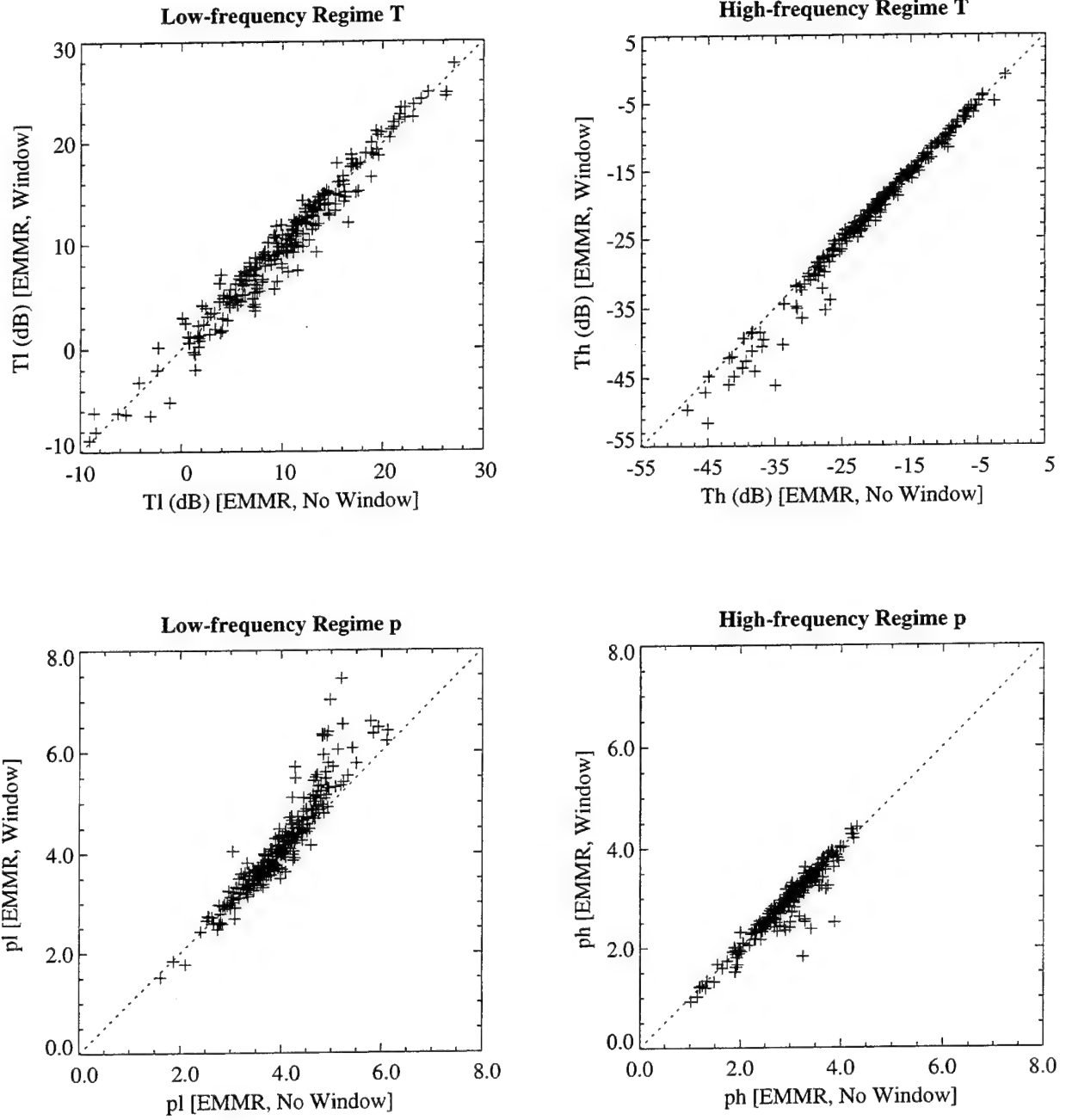
Figure 7: Comparison of strengths (top plots) and slopes (bottom plots) between Case 3 (EMMR, *no window; x* axis) and Case 2 (EMMR, *window; y* axis) processing.

windowing process involves multiplying the data sample to be passed to an FFT by some function that forces the data sample (and, depending on the window function, its first few derivatives) to zero at the ends of the sample. This is done to avoid spectral leakage, a problem identified in the original Wideband processing [*Fremouw et al.,* 1989]. In doing this, however, there is the possibility of introducing spurious power at the largest scales in the spectrum (*ie.,* across the size of the window).

The comparison between Case 2 and Case 3 in Figure 7 (windowed versus non-windowed) shows the two to be very similar, with the exception of (1) a tendency for the p_l values from the windowed analysis (along the y axis) to be higher than those from the non-windowed analysis (along the x axis) for the steepest observed slopes ($p_l > 5.0$), and (2) a tendency for the windowed T_h values to be lower than the non-windowed T_h values. A more detailed analysis showed that nearly all of the spectra that showed steeper slopes also showed lower values of T_h.

In looking at individual spectra, this effect is seen almost exclusively in spectra from samples in which there is very little scintillation. There is a very steep slope in the low-frequency section of the spectrum, with the high-frequency section at, or very near to, the noise floor. In comparing spectra from the windowed and non-windowed processing, it became apparent that the difference in slopes was due to spectral leakage from the very largest (almost DC) scales, which is most severe in the non-windowed spectrum. In the extreme case (no scintillation), the resulting spectrum is strongly dependent on the spectrum of the window, and any analysis of the spectral slopes will be contaminated by the shape of the spectrum of the window used.

Our final decision was to use the end-matched, mean-removal detrending method and to window the data. In order to remove contamination from the window as described in the previous paragraph, we excluded all results for cases where T_h was below -33dB (set based on inspection of Figure 7). With these spectra removed, the average values for the parameters given in Table 1 are $T_l = 11.0 \pm 5.7$, $p_l = 4.00 \pm 0.79$, $T_h = -18.6 \pm 7.1$, and $p_h = 2.94 \pm 0.65$. The results presented in the remainder of this report are based on this processing procedure.

Our selection of the frequency ranges over which to calculate the spectral fits was determined in an iterative process. It was initially based on visual inspection of L-band full-pass spectra generated for all of the Wideband passes available. Figure 8 shows an example of a full-pass PDS, in this case for a fairly disturbed pass (KW–18112 on 30 June 1979). The phase data were detrended using the Butterworth filter with a 180-s detrend period [the effect of the detrender can be seen clearly in the steep roll-off in the low-frequency end of the PDS plot (at $\log f < -2.0$)]. We noticed that there appeared to be a noticeable "break" in many of the full-pass spectra near 0.1 Hz. Thus, we set the fit range to separate the two fits at this frequency. Figure 9 shows the PDS plot with the two fits plotted over the full-pass spectrum from Figure 8 and the results of the fits (T and p from both fits) listed on the plot. We then moved on to look at other aspects of the processing using 0.1 Hz as the separation frequency for the two fits.

Wideband Pass KW-18112 (L-band)

Entire Pass

RMS: 10.89

Center Time: 46847
Sample size (sec): 655.36

Phase Power Density Spectrum

6020.0 km   19.0 km   60.2 m   At 500km (Veff)
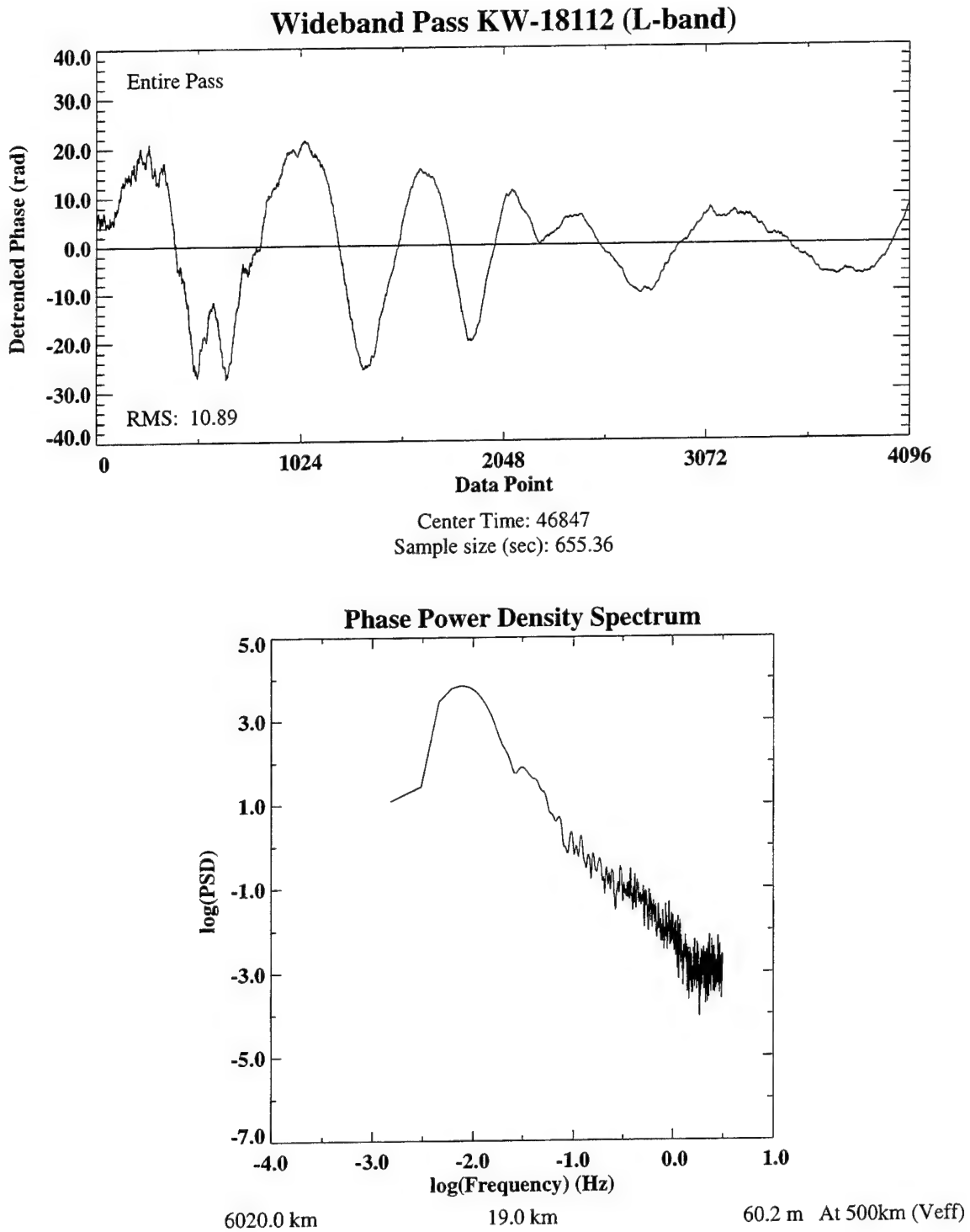
Figure 8: Detrended phase (upper plot) and phase spectrum (lower plot) for Wideband pass KW–18112. The numbers below the PDS plot are scale sizes corresponding to the frequencies on the x axis directly above them, calculated from the pass-averaged effective scan velocity (v_{eff}) at the 500-km ionospheric penetration point.

Phase Power Density Spectrum

TL: 1.73E-04
pL: 3.74
TH: 9.36E-03
pH: 2.06

6020.0 km   19.0 km   60.2 m   At 500km (Veff)
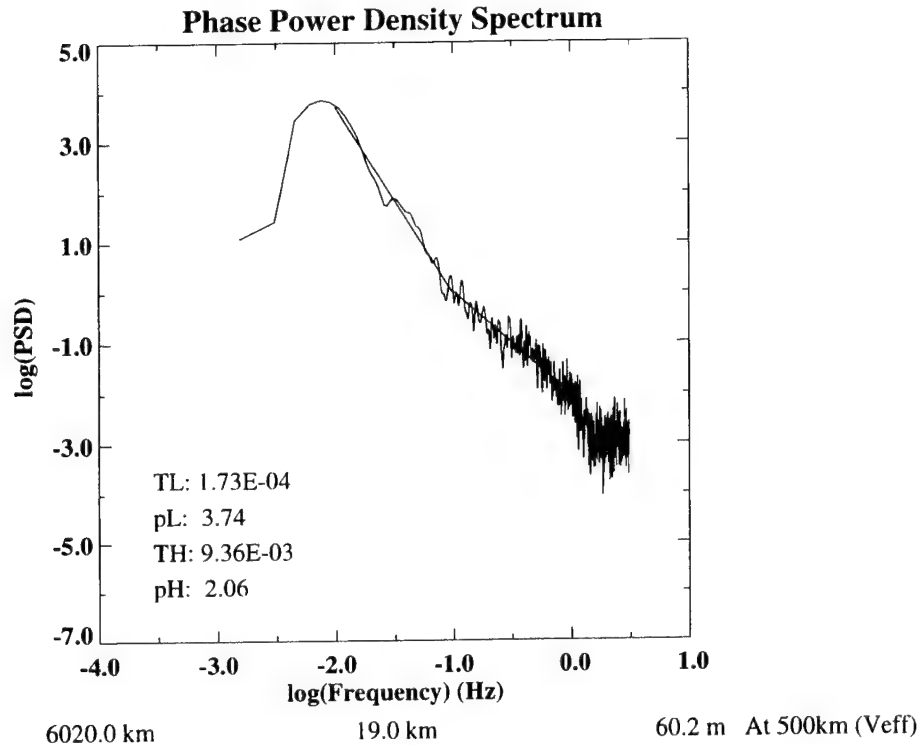
Figure 9: PDS plot from Figure 8 showing the results of the two PDS fits.

When we settled on other aspects of the processing, we returned to the issue of the fit ranges. Although developing an algorithm to find breaks in the spectra was beyond the scope of this effort, we did develop a simple algorithm based on the technique used in the original HiLat and Polar BEAR processing for locating the noise floor in spectra. The algorithm is fairly straightforward:

1. Resample the PDS at 50 points equally spaced in $\log f$.

2. Step through the PDS frequency range, generating a linear least-squares fit from equal-length (in $\log f$) subsets of the resampled PDS. In other words, if the number of $\log f$ bins used in the subsets is N, the first fit is generated using the PSD values from bins 1 through N, the second fit from bins 2 through $N + 1$, and the i-th fit from bins i through $i + N - 1$.

3. Track the slopes of the subsample fits (denoted p_i). If the magnitude of the slope begins to decrease (p is less negative), flag the frequency of the last PDS bin used in the subset that produced the most recent fit as the break frequency. Using the

21

notation from the previous paragraph, if $p_i > p_{i-1}$, then the break frequency is set to the frequency corresponding to bin $i + N - 1$.

4. The break frequency is converted to a break scale size using the average v_{eff} [calculated at the 500 km ionospheric penetration point (IPP)] over the sample size used to generate the original spectrum.

While no attempt was made to fine-tune this algorithm, we did check for the effects of altering the length of the PDS subsets (*ie.*, number of bins in the resampled PDS) used, and settled on 10 after a short study. We also did not conduct a rigorous test to ensure that this algorithm was stable over a wide range of spectral shapes, but in the few cases examined in detail the algorithm performed well.

Figures 10 and 11 show histograms of the break frequency and break scale, respectively, derived from analysis of 252 L-band spectra (192-s samples, not entire passes). (The gaps in Figure 10 are due to the discrete frequencies in the PDS's from which the f_b values were derived.) The average value for $\log f_b$ from the full set of 252 spectra was -0.96 with a variance of 0.11, and the average for x_b was 5.5 km with variance 2.7 km.

As a result of this analysis, we decided to continue to use 0.1 Hz as the separation frequency for the upper and lower spectral fits. The selection of 0.01 Hz as the low-frequency end of the lower-region fit and 1.0 Hz as the high-frequency end of the upper-region fit were based on visual inspection of a number of spectra. The criteria used were to avoid problems with detrender (and window) effects at the low-frequency end and to avoid the noise floor and the first Fresnel null at the high-frequency end.

The next issue is the definitions of T_l and T_h, the PSD strengths derived from the two least-squares fits. The original Wideband-derived T parameter was defined as the power spectral density at 1.0 Hz, *ie.*, the intercept from the fit to $\log \mathrm{PSD}$ as a function of $\log f$. Since the Wideband processing fit the spectra over the frequency range from 0.5 to 10.0 Hz, this placed the frequency at which T was defined within the fit range. In the current processing, our fits are over frequency ranges of 0.01 to 0.1 Hz and 0.1 Hz to 1.0 Hz, respectively. If we were to define T_l and T_h at 1.0 Hz, which is well outside the range of the low-frequency fit and at the high-frequency limit of the high-frequency fit, a "lever-arm" effect of extrapolating along the slope derived from the fit to 1.0 Hz could introduce a spurious correlation between the slope and the spectral strength. This same effect led us to redefine the height-integrated strength parameter used in our modeling from a scale size of 2π meters to 1.0 kilometer [*Robins et al.*, 1986]. We have therefore chosen to define these two strength parameters at the frequencies in the center of the $\log f$ range over which the fits are performed. Thus, T_l is defined at $\log f = -1.5$ and T_h is defined at $\log f = -0.5$.

3.2 Data Analysis. The primary goal of this task was to seek evidence for steeper slopes in the Wideband phase records than were found in the initial analyses of these data. As can be seen in both Table 1 and Figures 6 and 7 in the previous section, we have indeed
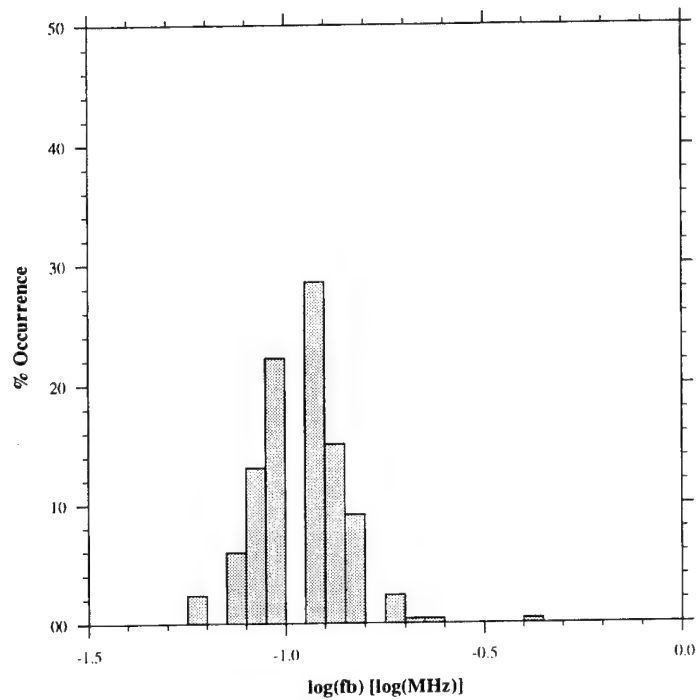
Figure 10: Histogram of PDS break frequencies derived from 252 Wideband L-band spectra.
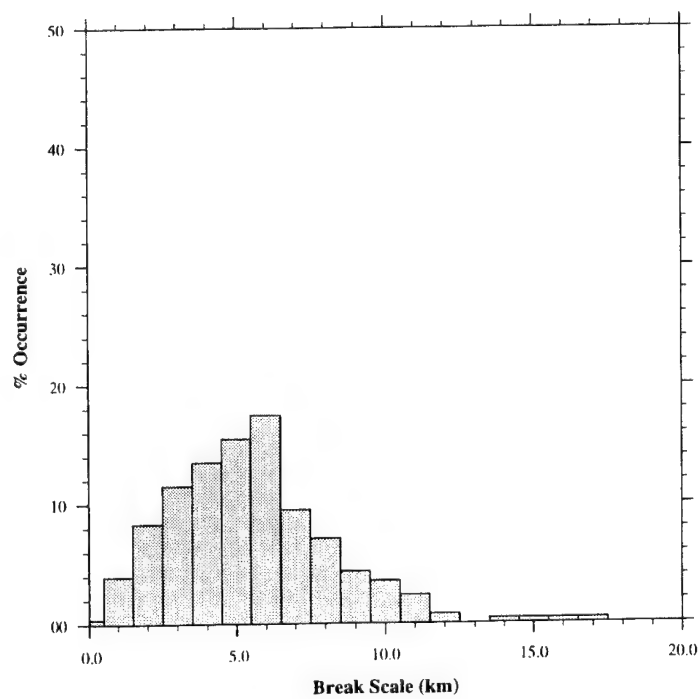

Figure 11: Histogram of PDS break scales derived from 252 Wideband L-band spectra.

such evidence. The average spectral slope found in the low-frequency spectral regime $(-2.0 \leq \log f \leq -1.0)$ is 3.99, and the average in the high-frequency spectral regime $(-1.0 \leq \log f \leq 0.0)$ is 2.96, both significantly steeper than the value of 2.5 used in the present WBMOD model. When the same analysis procedures were used to reprocess the VHF data, we obtained average slopes of 3.91 in the low-frequency regime and 2.23 in the high-frequency regime. In this case, the average slope in the high-frequency regime is closer to the WBMOD value.

The plots in Figure 12 summarize the results of our analysis. These plots show the spectral slope as a function of spectral strength in the low- and high-frequency regimes for both L band (upper plots) and VHF (lower plots). The solid lines in the plots are from a least-squares fit of the data, with the resulting equation shown in the upper right of each plot and the correlation coefficient in the lower left. The two plots from the low-frequency regime show little correlation between the slope and the strength at both L band and VHF. In the high-frequency regime, however, the L band results show only a slight correlation between slope and strength, while the VHF results show a significant correlation between the two.

This correlation between spectral slope and strength was first noted in *Livingston et al.* [1981], based on analysis of Wideband VHF spectra. Figure 13 shows results reported in that paper (their Figure 11) and the VHF high-frequency regime results from the present analysis plotted on the same axis ranges. Note that the T_h values used in this figure differ from those in Figure 12 in that they have been redefined from $\log f = -0.5$ to $\log f = 0.0$, the spectral frequency at which the *Livingston et al.* [1981] T values were defined. The equation of the least-squares fit to the *Livingston et al.* [1981] data is $p = -0.03T + 2.1$, which is nearly identical to that obtained in the present analysis ($p = -0.031T + 1.91$). Thus, the results we have obtained in the high-frequency regime of the VHF phase spectra are in general agreement with earlier analyses of (essentially) the same data. The average slope of 2.5 reported in *Livingston et al.* [1981] was one input to the original decision to set $p = 2.5$ in the equatorial region in the WBMOD model.

We believe that the shallower slopes seen in the VHF data and the apparent correlation between p and T in Figure 13 are caused by diffraction effects on the high-frequency section of the phase spectra. Since the analyses leading to the selection of a spectral slope of 2.5 used fits to the high-frequency sections (0.5 to 10.0 Hz) of the VHF spectra, that selection was strongly biased by the effects of diffraction (effects which the WBMOD model is not designed to include). The dependence of p on T is apparently a transition from spectra dominated by weak-scattering effects (with characteristic slopes ~ 4.0) to spectra increasingly contaminated by diffraction effects as conditions move into the strong-scatter regime (with characteristic slopes ~ 2.0). Our decision to use only the L-band data in our analysis was based on our desire to minimize these diffraction effects on our final result.

There was some concern about diffraction effects on the phase spectra during the early analysis of the Wideband data, but studies of the p and T data generated from the standard Wideband processing appeared to show that the effects were small [Rino et al., 1978]. In
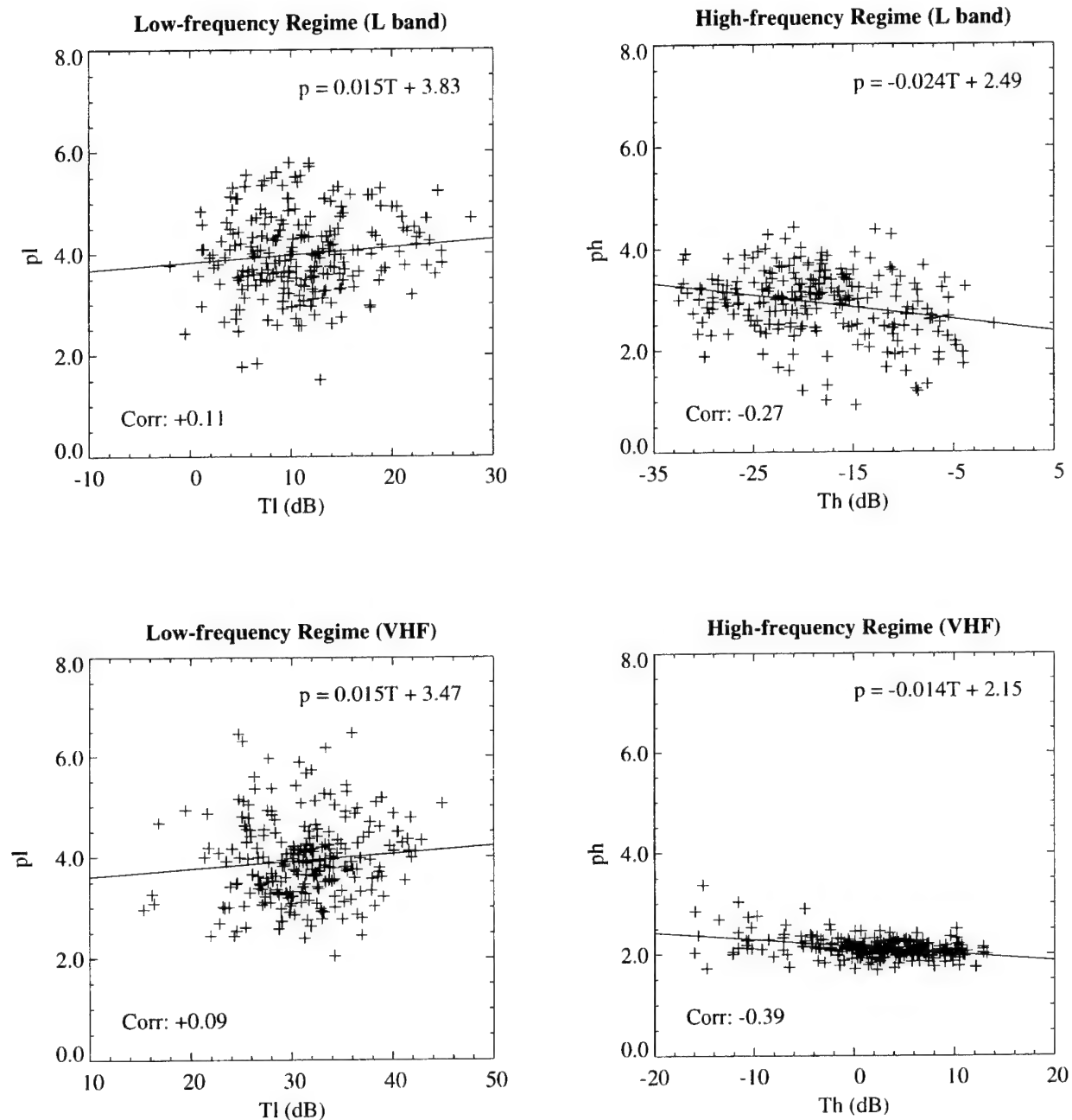
Figure 12: Variation of slope as a function of spectral strength at L band (upper plots) and VHF (lower plots). The left-hand plot in each set is for the low-frequency regime, and the right-hand plot for the high-frequency regime. The solid lines are least-squares fits to the data, with the fit equation shown in the upper right corner of each plot and the correlation coefficient in the lower left corner.

25
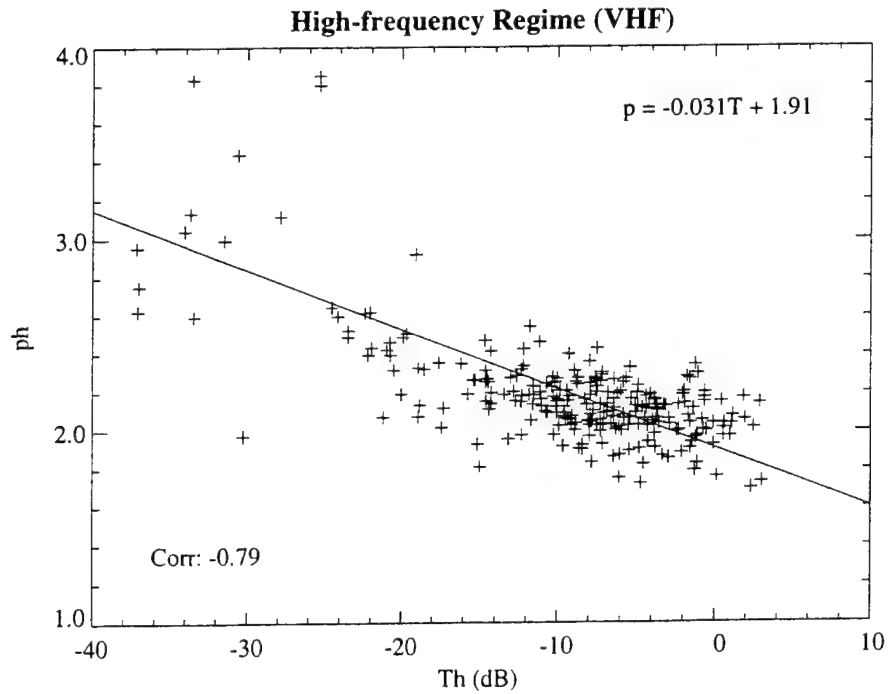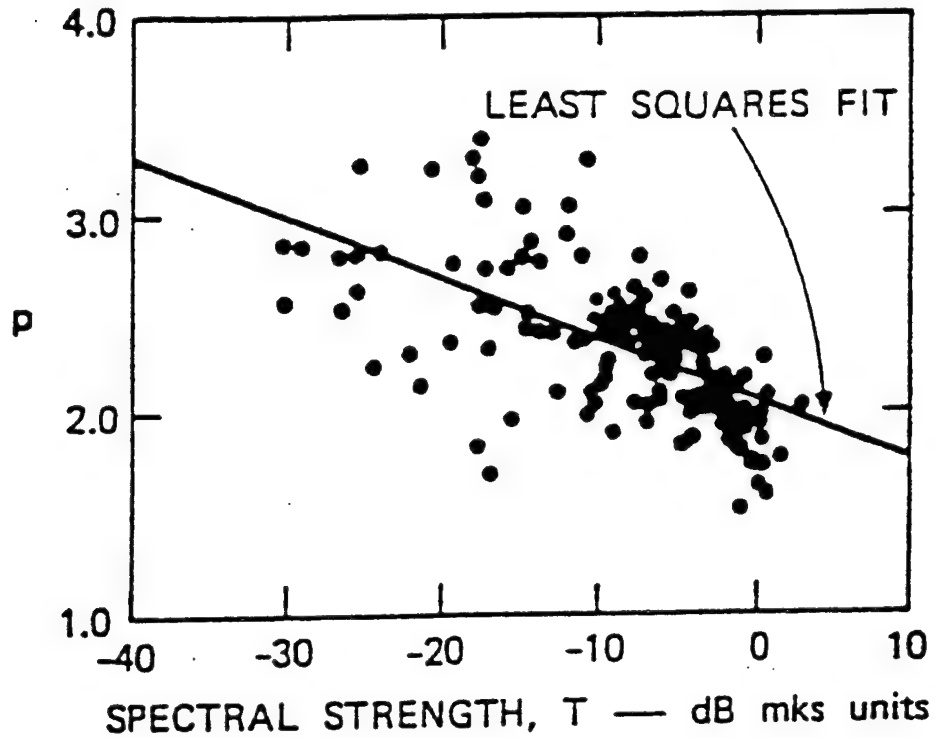
Figure 13: Variation of spectral slope as a function of spectral strength from *Livingston et al.* [1981] (upper plot) and from our high-frequency regime VHF analysis (T_h redefined to 1.0 Hz) (lower plot). The solid lines are from linear least-squares fits to the data.

preparing for the HiLat satellite launch, we found that there were shortcomings in the routine Wideband processing that could contaminate the spectra from which p and T were derived. Two of these, inadequate tracking of phase "ramping" (cycle slips) and not windowing the detrended phase records prior to processing them with an FFT, resulted in spectral-leakage problems that led to underestimates of p and over-estimates of T [*Fremouw and Secan*, 1982]. It is quite possible that these processing shortcomings masked the diffraction effects we have found here.

With regard to the objective of this task, we have confirmed that the Wideband data support steeper slopes in the phase spectra, with an average slope ~ 4.0 at larger scales (> 10 km) and ~ 3.0 at smaller scales (ignoring diffraction effects). This is in agreement with the Brown data that prompted this study.

3.3 Development of Two-Regime Spectrum Model. Development was begun on a two-regime power-law PDS model for implementation in WBMOD at some future time. Models for the parameters required to characterize the two-regime PDS for WBMOD are to be derived from a more detailed analysis of data from the various latitude regimes (equatorial, mid-latitude, high-latitude) similar to that described in the previous section.

We take the 3-D spectrum of plasma density, which comprises a total variance $\langle (\Delta N_e)^2 \rangle$, to be the sum of two power-law components. The first, containing variance $\langle (\Delta N_e)_h^2 \rangle$, is a high-frequency component defined by its PSD, C_h, evaluated at a cross-field (and cross-b) wavenumber of $\kappa_h = 2\pi/10^3$ rad/m and by a logarithmic slope $p_h + 1$. The other, containing variance $\langle (\Delta N_e)_l^2 \rangle$, is a low-frequency component defined analagously by a slope $p_l + 1$ and a strength, C_l, defined at a wavenumber $\kappa_l = 2\pi/10^4$ rad/m as follows:

$$C_l = 8\pi^{3/2} \frac{\Gamma\left(\frac{p_l+1}{2}\right)}{\Gamma\left(\frac{p_l-2}{2}\right)} \langle (\Delta N_e)_l^2 \rangle \frac{\kappa_o^{p_l-2}}{(\kappa_o^2 + \kappa_l^2)^{(p_l+1)/2}} \quad , \tag{2}$$

where κ_o is an outer-scale wavenumber.

The temporal spectrum of phase, $P_\phi(f)$, then becomes the sum of the following two components:

$$P_l(f) = T_l \frac{(f_o^2 + f_l^2)^{p_l/2}}{(f_o^2 + f^2)^{p_l/2}} \quad , \text{ and} \tag{3}$$

$$P_h(f) = T_h \frac{(f_o^2 + f_h^2)^{p_h/2}}{(f_o^2 + f^2)^{p_h/2}} \tag{4}$$

where T_h is defined at $f_h = 1$ Hz and where

$$f = V_e \kappa / 2\pi \quad , \text{ and}$$

$$f_o = V_e \kappa_o / 2\pi = V_e / 2\pi\alpha \quad ,$$

with V_e being the effective (*ie.*, cross-field and cross-b) velocity.

Proceeding in a fashion analagous to Appendix A of *Robins et al.* [1986], we define T_l at $f_l = 1/60$ Hz $= 16.67$ mHz, as follows:

$$T_l = \frac{r_e^2 \lambda^2 \sqrt{\pi}}{(2\pi)^{(p_l+1)}} \frac{\Gamma\left(p_l/2\right)}{\Gamma\left(\frac{p_l+1}{2}\right)} L \sec\theta G C_l \frac{(\kappa_o^2 + \kappa_l^2)^{(p_l+2)/2}}{(f_o^2 + f_l^2)^{p_l/2}} V_e^{(p_l-1)} \quad , \tag{5}$$

where all variables not defined herein carry their usual definitions. With $\alpha = 10^6$ m and $\kappa_l = 2\pi/10^4$ rad/m we have $\kappa_o \ll \kappa_l$, $f_o \ll f_l$ and, with good approximation,

$$T_l = (r_e\lambda)^2 \frac{(60)^{p_l} \sqrt{\pi}}{(10^4)^{(p_l+1)}} \frac{\Gamma\left(p_l/2\right)}{\Gamma\left(\frac{p_l+1}{2}\right)} G \sec\theta V_e^{(p_l-1)} C_l L \quad . \tag{6}$$

If we impose a cutoff at $f_c = 1/180$ Hz $= 5.556$ mHz, we have $f_o \ll f_c < f_l \ll f_h$ and, from [3] and [4],

$$\sigma_\phi^2 = 2 \int_{f_c}^\infty \left[T_l \frac{(f_o^2 + f_l^2)^{p_l/2}}{(f_o^2 + f^2)^{p_l/2}} + T_h \frac{(f_o^2 + f_h^2)^{p_h/2}}{(f_o^2 + f^2)^{p_h/2}} \right] df \tag{7}$$

$$\sigma_\phi^2 \approx 2 T_l f_l^{p_l} \int_{f_c}^\infty f^{-p_l} df + 2 T_h f_h^{p_h} \int_{f_c}^\infty f^{-p_h} df = \frac{2 T_l}{p_l - 1} \frac{f_l^{p_l}}{f_c^{p_l-1}} + \frac{2 T_h}{p_h - 1} \frac{f_h^{p_h}}{f_c^{p_h-1}} \quad . \tag{8}$$

In practice, we do not have access to the two spectral components separately. To measure T_l and T_h directly from the component spectrum, we must assume that $T_l \approx P_\phi(f_l)$ and $T_h \approx P_\phi(f_h)$, which requires that $P_l(f_l) \gg P_h(f_l)$ and $P_h(f_h) \gg P_l(f_h)$. The practical requirement corresponding to the conditions $P_l(f_l) \gg P_h(f_l)$ and $P_h(f_h) \gg P_l(f_h)$ is as follows:

$$\log\left(\frac{f_l}{f_h}\right) \ll -\frac{1}{p_h} \log\left(\frac{T_l}{T_h}\right) \qquad \text{for} \quad P_l(f_l) \gg P_h(f_l) \quad , \tag{9}$$

and

$$\log\left(\frac{f_l}{f_h}\right) \ll -\frac{1}{p_l} \log\left(\frac{T_l}{T_h}\right) \qquad \text{for} \quad P_h(f_h) \gg P_l(f_h) \quad . \tag{10}$$
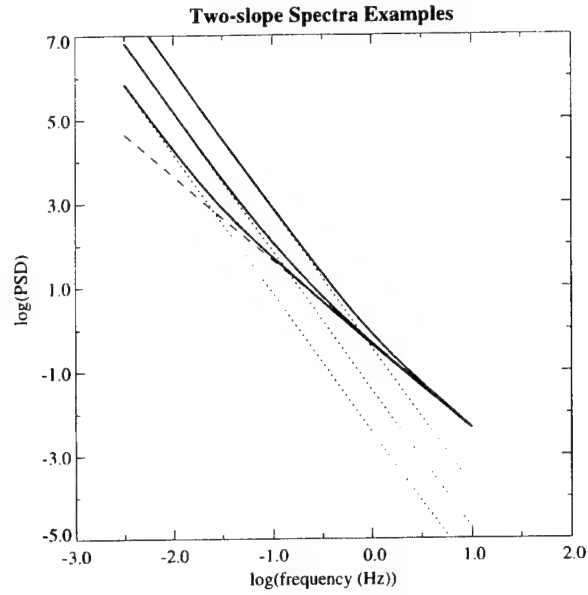
Figure 14: Samples of the two-regime PDS model with $f_l = 0.0167$ Hz, $p_l = 4.0$, and $p_h = 2.5$.
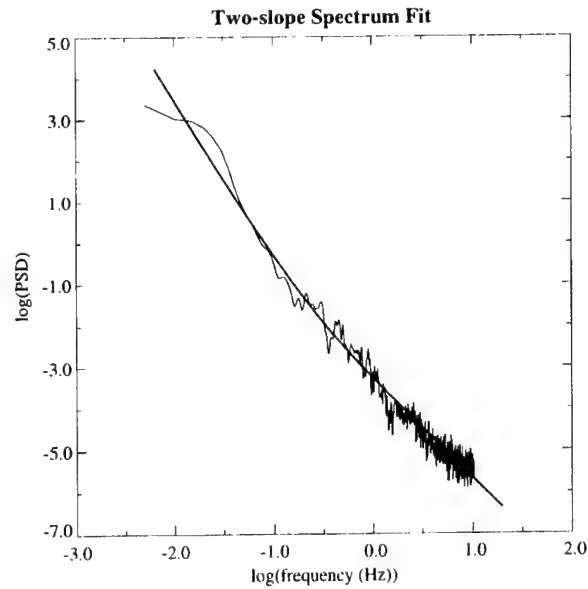

Figure 15: Example of the result of fitting the two-regime PDS model (heavy solid curve) to an observed L-band phase PDS (light solid curve).

Since we expect that $p_l \geq p_h$, meeting [9] ensures that [10] is met.

Three examples of two-slope spectra, with $p_l = 4.0$ and $p_h = 2.5$ and with different values of the ratio T_l/T_h, appear on Figure 14. The composite spectra are represented by heavy solid curves, and their corresponding low-frequency components are indicated as dotted lines. The dashed curve represents the high-frequency component. Note that the condition $P_h(f_h) \gg P_l(f_h)$ is barely met for the upper curve (corresponding to $T_l/T_h = 10^6$) and that the condition $P_l(f_l) \gg P_h(f_l)$ is not fully met for the middle curve ($T_l/T_h = 10^5$) and is definitely violated for the lower curve ($T_l/T_h = 10^4$). Thus, T_l and T_h should be measured on component fits obtained from frequency ranges as low and as high, respectively, as possible rather than directly from the composite spectrum. Moreover, we should employ an f_l as much below f_h (1 Hz) as possible. Note that the plot also illustrates a working definition of break frequency, f_b, as the frequency at which P_l and P_h are equal, or $P_h(f_b) = P_l(f_b) = P_\phi(f_b)/2$.

We have also developed an initial algorithm for fitting this two-regime model to observed spectra. An example of the result of such a fit is presented in Figure 15, which shows an L-band spectrum (light solid curve) with the two-regime model fit plotted over it (heavy solid curve). This algorithm starts with the T and p values derived from linear fits to the upper and lower sections of the PDS, and then uses a non-linear least-squares fitting technique to achieve the best fit of the two-regime model to the spectrum.

REFERENCES.

Bishop, G., Walsh, D., Daly, P. Mazzella, A., and Holland, E., Analysis of the temporal stability of GPS and GLONASS group delay correction terms seen in various sets of ionospheric delay data, *Proceedings of ION GPS-94*, 1653-1661, Institute of Navigation, Alexandria, VA 1994.

Fremouw, E. J., and J. A. Secan, Preparation for the polar beacon satellite mission (HiLat), *Progress Report No. 8*, Contract No. DNA0001–81–C–0189, Northwest Research Associates, Inc., Bellevue, WA, 1982.

Fremouw, E. J., J. A. Secan, and J. M. Lansinger, Anisotropy effects on and other characteristics of high-latitude scintillation, *Report DNA-TR-88-77*, Defense Nuclear Agency, Washington, DC, 1989.

Fremouw, E. J., C. C. Andreasen, and J. A. Secan, Investigations of ionospheric Total Electron Content and scintillation effects on transionospheric radiowave propagation, *Proposal NWRA–CR-94–P223*, Northwest Research Associates, Inc., Bellevue, WA, 1994.

Livingston, R. C., C. L. Rino, J. P. McClure, and W. B. Hanson, Spectral characteristics of medium-scale equatorial F region irregularities, *J. Geophys. Res.*, *86*, 2421-2428, 1981.

Rino, C. L., R. C. Livingston, M. D. Cousins, B. C. Fair, and M. J. Baron, in *Effect of the Ionosphere on Space and Terrestrial Systems,* edited by J. Goodman, pp. 2-9, US Government Printing Office, Washington, DC, 1987.

Robins, R. E., J. A. Secan, and E. J. Fremouw, A mid-latitude scintillation model, *Report DNA–TR–86–381,* Defense Nuclear Agency, Washington, DC, 1986.

Secan, J. A., Bussey, R. M., E. J. Fremouw, and L. A. Reinleitner, An investigation of methods for improving models of ionospheric plasma-density irregularities and radio-frequency scintillation, *Report PL–TR–93–2005,* ADA276689, Phillips Laboratory, Hanscom AFB, MA, 1993.

THIS PAGE INTENTIONALLY LEFT BLANK

Appendix A. Final Report From RDP.

This appendix contains the verbatim text of the final report received from RDP, Incorporated, describing the work they completed on this project under subcontract to NWRA.

Description of the Problem

Ranging signals from satellites of the Global Positioning System (GPS) are subject to both local and distant environmental influences, as well as transmitter and receiver effects, which affect the utilization of this system. An algorithm has been developed for determining combined satellite and receiver bias values using ionospheric measurement data, while also generating an accurate representation of the ionospheric Total Electron Content(TEC) in location and time (Bishop, et al.) [1]. This algorithm has been applied to TEC measurements from a number of different sites, and to GLONASS observations as well as those GPS satellites. The validity and robustness of the algorithm has been demonstrated, but there are a few deficiencies for large-scale processing of data from many sites. Among these are the extensive computational time required by the method for evaluating a day of data, the numerous manual preparatory steps for processing the data, the sensitivity of the method to occasional discontinuities in the measurements, and reliance of the algorithm on the quasistationary behavior of the ionosphere. The principal efforts were to make algorithm and processing refinements to help remedy these deficiencies.

Description of the Effort

Initial support was provided for satellite and receiver bias determinations using the algorithm and software developed during the summer of 1994. Earlier results were re-evaluated in an attempt to resolve discrepancies between PL Hanscom and JPL Westford data for the same dates, but no definite conclusions were obtained.. A procedure was developed to plot derived vertical TEC profiles for a set of adjoining latitude bands as part of this investigation.

The database generation, bias calculation, and TEC profile plotting procedure was standardized for general applicability to multiple receiver sites, using site-specific information in separate files when necessary. A refined method for bias calculations was developed, replacing the earlier minimization search process by a system of coupled linear equations. The refined method requires only one pass through the data to determine the coefficients and inhomogenous terms of the linear equations, and significantly reduces the time required to perform the calculation. The refined method was applied to the Ionospheric Monitoring System (IMS) operating at Otis Air National Guard Base, to validate its operation.

A number of investigations were performed to evaluate the results from the IMS at Otis and to improve the processing of data from that system. The general data listing program was modified to report the satellite and receiver biases in nanoseconds of delay, with provisions to select any of the three data record types (raw data, 1-minute data, or 15-minute data) individually of jointly. This program was utilized to determine the cause of anomalous high TEC values appearing in the 15-minute reports being transmitted to Air Weather Service, and to validate the usage of the satellite and receiver biases were added as output values to the conversion program which generates the initial data files for the bias determination

---

[1] Bishop, G. J. and Holland, E. A., Apparent Good Temporal Stability of the GPD Group Correction Term Seen in Two Large Sets of Ionospheric Delay Data, American Geophysical Union, December 1993.

process, although the complete utilization of these biases has not yet been implemented. Some of the anomalous TEC values were attributed to significant initial discrepancies in the measured differential group delay, contributing to a major phase averaging error, which diminished with time, but other unusual TEC values were associated with spurious satellite observations, which have provisionally been dubbed "ghosts". A preliminary characterization of these was developed, but further investigation was required.

A set of satellite and receiver biases was defined for the Otis IMS on 13 February 1995, using measurements performed on 23 January 1995. These biases were derived using the bias determination method to calculate correction values for the initial biases established for the IMS, with the appropriate transformations for transmitter group delay being applied to the satellite biases. The resulting TEC values were monitored on several subsequent dates, employing procedures similar to those used in processing the data for bias determination, and the results were generally reasonable, although some further bias adjustments were considered.

A significant disruption to the standard Otis IMS processing and maintenance was the termination of the tape archival process due to an error status. This also disrupted the regular data transfer to the disk archival directory, so immediate intervention was required to preserve the existing data, and an interim procedure was developed to re-establish the disk archive. This procedure is still operational, but requires a manual initialization after each restart.

Support was provided for the installation and testing of a second IMS and associated mini-computer at Croughton, England. The bias determination procedures were augmented by procedures for data pre-processing and ephemeris conversion, and all procedures were installed, tested, documented, and demonstrated to convert the results obtained from the bias determination to the appropriate quantities and format for utilization by the IMS. Further procedures were implemented to process data from a receiver and notebook PC system obtained from Applied Research Laboratories at the University of Texas, Austin, to be operated concurrently with the Croughton IMS during the initial testing period. Remote communications were established with both the IMS and the mini-computer during their initial operation at Croughton.

The bias determination procedure was applied to a number of days of data from Shemya for 1992, to test the method for the ionospheric characteristics for this site and to corroborate earlier results derived by a different technique. Some parametric revisions for the Ionospheric Penetration Point latitude range and observation conjunction weighting were required to appropriately associate measurements from all of the observed GPS satellites, but the method produced excellent results.

A preliminary investigation was performed to apply the bias determination method to single-frequency GPS measurements. For this investigation, a new data pre-processor was developed to derive slant TEC measurements from single-frequency pseudo-range and Doppler

measurements, and the bias calculation program was revised to retain distinctions between different pass segments of the same satellite. The processing of true single-frequency data was unsatisfactory, apparently due to lack of accuracy in the time tags assigned to the measurements samples, but a similar procedure applied to unreferenced differential phase data produced very good results for the derived ionospheric diurnal profile.

Further analysis was performed to evaluate the errors associated with the Total Electron Content (TEC) calculation for a single-frequency GPS receiver, and plots were generated demonstrating the correlation of TEC errors with variations in the time tag for the data samples. A memorandum describing the analysis and conclusions was drafted for the vendor of the receiver.

Recent data were retrieved from the Ionospheric Monitoring System (IMS) at Otis. These data were used to evaluate the performance of the current bias definitions for the Otis IMS and to calculate corrections and revised bias values for installation on the Otis IMS. These data were also reviewed for anomalous and spurious TEC measurements, as part of the continued assessment of the IMS performance.

Specifications were defined for possible improvement of the bias determination algorithm, using parametric values which emphasize apparent Ionospheric Penetration Point (IPP) conjunctions in latitude and local time for different GPS observations, in contrast to the current values which apply nearly uniform weighting over all IPP observations in a narrow latitude band.

Appendix B. Pass Tables.

The tables in this appendix summarize information for the satellite data used in the analysis described in Section 3. The passes are ordered by satellite (HiLat, Polar BEAR, or Wideband), location (Kwajalein or Ancon), and date. The first column shows the designator for a pass, which includes the location (KW or AN) and the GMT date/time (DDDHH) at the start of the pass. For each pass, these tables list the date of the pass, the start and end times of the pass (GMT), the length of the pass (m:s), and the maximum elevation angle for the entire pass (degrees).

Table 2: Summary of passes included in the analysis.

| Pass Designator | Start | | | Pass Length | Maximum Elevation |
	Date	Time (UT)	Time (LT)		
	HiLat Passes — Kwajalein				
KW–19911	860718	11:38:23	22:41:14	14:15	88.4
KW–20011	860719	11:12:19	22:33:47	14:00	56.1
KW–20110	860720	10:46:30	22:26:49	12:45	33.8
KW–20210	860721	10:20:56	22:20:22	11:15	20.8
KW–20212	860721	12:02:26	22:20:51	11:45	26.1
KW–20311	860722	11:35:11	22:10:58	13:45	42.6
KW–20411	860723	11:08:48	22:02:51	14:15	71.1
KW–20510	860724	10:43:17	21:56:32	13:30	70.9
KW–20610	860725	10:17:19	21:49:17	13:15	42.4
KW–20709	860726	09:51:19	21:41:58	11:45	25.9
KW–20711	860726	11:33:46	21:44:19	5:45	20.9
KW–20811	860727	11:10:14	21:41:50	8:30	33.8
KW–20910	860728	10:39:35	21:25:17	12:45	56.2
KW–21612	880803	12:58:41	00:23:35	8:00	59.5
KW–21712	880804	12:32:03	00:15:09	4:30	34.8
KW–21913	880806	13:21:24	00:01:23	8:00	40.3
KW–22012	880807	13:01:21	00:07:34	1:15	9.9
KW–22112	880808	12:29:54	23:48:29	7:00	70.7
KW–22212	880809	12:03:10	23:40:02	6:00	42.2
KW–22412	880811	12:52:39	23:26:38	6:30	31.9
KW–22512	880812	12:25:57	23:18:17	5:45	54.7
KW–22611	880813	11:59:09	23:09:42	6:30	87.9
KW–22711	880814	11:34:23	23:05:17	5:45	42.1
KW–22811	880815	11:07:40	22:56:53	5:45	29.0
KW–22912	880816	12:21:53	22:47:51	2:00	26.5
KW–23011	880817	11:55:07	22:39:20	6:45	44.1
KW–23111	880818	11:30:24	22:35:04	5:45	53.1
KW–23211	880819	11:03:37	22:26:31	6:30	56.5
KW–23309	880820	09:48:58	19:58:20	4:45	19.5
KW–23310	880820	10:37:50	22:20:03	5:30	32.1
KW–23410	880821	10:10:09	22:09:39	6:00	22.4
KW–23411	880821	11:51:05	22:09:02	7:00	21.4
KW–23511	880822	11:26:20	22:04:41	6:00	32.4
KW–23610	880823	10:59:53	21:56:51	5:45	51.3
KW–23710	880824	10:32:52	21:47:50	6:30	75.6
KW–23810	880825	10:06:09	21:39:26	7:00	46.0

Table 2: Summary of passes included in the analysis (cont).

Pass Designator	Start			Pass Length	Maximum Elevation
	Date	Time (UT)	Time (LT)		
KW–23909	880826	09:41:29	21:35:17	4:30	23.2
KW–24010	880827	10:55:37	21:26:05	6:15	28.0
KW–24110	880828	10:29:19	21:18:34	6:15	45.7
KW–24210	880829	10:02:05	21:09:07	7:15	83.9
Polar BEAR Passes — Kwajalein					
KW–21410	880801	10:54:19	21:16:57	7:15	27.5
KW–21610	880803	10:06:21	21:08:28	12:15	68.1
KW–21710	880804	10:37:10	21:04:23	9:00	29.8
KW–21809	880805	09:20:23	21:00:15	12:45	49.8
KW–21909	880806	09:51:29	20:56:13	11:30	73.7
KW–22010	880807	10:22:02	20:52:05	9:30	32.2
KW–22109	880808	09:04:53	20:47:54	11:30	46.0
KW–22209	880809	09:35:29	20:43:48	11:30	79.4
KW–22310	880810	10:07:17	20:39:50	6:15	34.9
KW–22408	880811	08:49:19	20:35:32	12:15	42.6
KW–22509	880812	09:18:38	20:31:14	10:00	85.3
KW–22609	880813	09:49:37	20:27:11	11:00	37.8
KW–22708	880814	08:34:32	20:23:17	11:30	39.5
KW–22809	880815	09:02:49	20:18:50	12:15	88.7
KW–22909	880816	09:34:37	20:14:54	9:15	40.9
KW–23008	880817	08:20:44	20:11:08	9:30	36.6
KW–23108	880818	08:47:29	20:06:31	11:00	82.7
KW–23308	880820	08:03:25	19:58:34	11:00	34.0
KW–23408	880821	08:31:39	19:54:07	13:00	77.0
KW–23708	880824	08:16:01	19:41:45	9:00	71.4
KW–23719	880824	19:46:31	07:40:44	10:15	34.3
KW–23721	880824	21:31:37	07:40:27	7:45	19.5
KW–23820	880825	20:16:12	07:36:30	10:45	77.5
KW–23920	880826	20:46:04	07:32:17	10:15	47.7
KW–24019	880827	19:31:02	07:28:23	9:00	31.7
KW–24021	880827	21:15:55	07:28:04	8:30	21.1
KW–24120	880828	20:00:45	07:24:09	10:30	71.8
KW–24220	880829	20:30:32	07:19:56	10:15	51.5
Wideband Passes — Kwajalein					
KW–18912	770708	12:54:12	23:46:37	10:45	41.2
KW–20912	770728	12:14:05	23:42:48	9:30	80.5
KW–21212	770731	12:27:49	23:46:24	12:15	74.7

Table 2: Summary of passes included in the analysis (cont).

| Pass | Start | | | Pass | Maximum |
Designator	Date	Time (UT)	Time (LT)	Length	Elevation
KW–21613	770804	13:23:50	23:45:23	8:15	22.0
KW–22400	770812	00:20:20	11:32:57	12:00	67.0
KW–22404	770812	11:42:04	23:50:09	11:00	35.5
KW–22610	770814	11:19:19	23:37:35	8:45	23.2
KW–22613	770814	13:02:29	23:47:05	10:30	35.2
KW–22812	770816	12:36:59	23:47:01	11:45	61.6
KW–22911	770817	11:33:20	23:40:12	10:15	32.3
KW–22913	770817	13:17:40	23:47:00	9:15	25.5
KW–23211	770820	11:47:30	23:42:37	11:15	45.0
KW–23412	770822	11:23:30	23:38:34	9:30	25.8
KW–23512	770823	12:02:00	23:44:08	11:45	62.8
KW–23713	770825	13:22:30	23:47:06	8:45	23.3
KW–23812	770826	12:16:30	23:45:58	12:15	85.8
KW–24112	770829	12:31:30	23:46:28	11:45	70.4
KW–25011	770907	11:32:07	23:39:48	10:45	32.0
KW–16212	790611	12:37:40	23:56:14	11:45	75.0
KW–17012	790619	12:39:50	23:56:40	11:45	71.6
KW–17312	790622	12:53:49	23:57:20	10:15	52.4
KW–17812	790627	12:42:10	23:56:35	11:45	68.4
KW–18112	790630	12:56:10	23:56:59	11:15	50.0
KW–18312	790702	12:30:30	23:55:51	11:45	87.5
KW–18413	790703	13:10:20	23:56:57	10:45	36.5
KW–20212	790721	12:48:40	23:57:07	11:45	59.8
KW–21111	790730	11:46:30	23:51:03	10:45	34.8
KW–21113	790730	13:31:10	23:57:24	9:00	23.9
Wideband Passes — Ancon					
AN–04004	770209	04:41:29	23:28:46	12:45	55.0
AN–04204	770211	04:16:29	23:27:41	13:15	86.5
AN–04903	770218	03:42:09	23:24:50	12:00	39.8
AN–06304	770304	04:15:49	23:28:09	13:15	84.5
AN–07404	770315	04:35:59	23:28:05	10:45	63.9
AN–07503	770316	03:32:29	23:23:18	10:15	30.6
AN–07604	770317	04:10:59	23:27:27	12:00	75.0
AN–07803	770319	03:46:39	23:25:13	11:15	42.7
AN–07904	770320	04:25:49	23:27:58	12:00	80.1
AN–08003	770321	03:22:49	23:21:53	9:15	24.5
AN–08005	770321	05:06:09	23:28:00	10:30	32.5

Table 2: Summary of passes included in the analysis (cont).

| Pass | Start | | | Pass | Maximum |
Designator	Date	Time (UT)	Time (LT)	Length	Elevation
AN–08104	770322	04:01:09	23:25:40	11:45	60.4
AN–08204	770323	04:40:39	23:28:36	11:45	58.4
AN–08305	770324	05:21:39	23:28:10	9:15	24.0
AN–08504	770326	04:55:49	23:28:23	11:15	41.2
AN–08803	770329	03:27:19	23:21:36	9:45	27.7
AN–08805	770329	05:10:59	23:28:35	10:15	29.9
AN–08904	770330	04:05:40	23:26:18	12:15	66.9
AN–09603	770406	03:31:40	23:21:33	10:30	31.4
AN–10304	770413	04:39:50	23:29:24	12:15	60.4
AN–10403	770414	03:36:10	23:22:10	11:00	34.8